UNIVERSIDAD DE CONCEPCIÓN
FACULTAD DE CIENCIAS FÍSICAS Y MATEMÁTICAS
PROGRAMA DE MAGÍSTER EN ASTRONOMÍA

A RELATIONSHIP BETWEEN IRON SPREAD AND VARIABILITY IN GIANT STARS OF GLOBULAR CLUSTERS

(UNA RELACIÓN ENTRE DISPERSIÓN DE HIERRO Y VARIABILIDAD EN ESTRELLAS GIGANTES DE CÚMULOS GLOBULARES)

Profesor Guía: Dr. Sandro Villanova
Departamento de Astronomía
Facultad de Ciencias Físicas y Matemáticas
Universidad de Concepción

Tesis para ser presentada a la Dirección de Postgrado de la Universidad de Concepción para optar al grado de Magister en Astronomía

ÁLVARO IGNACIO LLANCAQUEO ALBORNOZ
Concepción - Chile
Enero 2020

Acknowledgements

Primero que todo quiero agradecer a mi profesor guía, Dr. Sandro Villanova por su guianza, su apoyo durante estos años y por haberme aceptado como su estudiante para este programa. Quiero agradecer además a Caddy Cortés, por haberme ayudado a lo largo de este tiempo, guiando y ayudándome en mi trabajo, otorgando comentarios, destacando los errores que tenía y dándome sugerencias sobre cómo avanzar en este trabajo

Por apoyarme tanto emocionalmente para seguir adelante en tiempos difíciles, su apoyo económico para que haya podido seguir estudiando en la Universidad de Concepción y más importante por tener fe en mí, quiero agradecer a mis padres Álvaro Llancaqueo Valeri y Edith Albornoz Rojas.

Por su apoyo y guía cuando tenia dudas relacionadas en cómo seguir y al practicar mis presentaciones, agradezco a mi profesora de Lenguaje de The Wessex School y amiga, Pamela Cebrero.

Quiero también darle las gracias a mis amigos de las comunidades "Yu-Gi-Oh! TCG" y "Cardfight!! Vanguard" de Concepción, en especial a Felipe Jarpa, Eduardo Ramirez, Carlos Becar, Hernán Rodriguez, Matias Valeria, Diego Soto, Mauricio Werlinger y Pablo Flores. Por su apoyo emocional, amistad y camaradería, además de escucharme de vez en cuando cuando hablaba de mi trabajo.

También agradezco a todos mis colegas, compañeros y miembros del Departamento de Astronomía de la Universidad de Concepción por su ayuda y contribuciones varias, especialmente durante el último año del programa. Quiero hacer una mención especial a mis amigos que estuvieron conmigo durante mi formación académica en pregrado desde el 2014 al 2017: Matias Cruces, Juan Arévalo y Javier Henríquez.

Por último quiero darle las gracias a aquellos que colaboraron en este trabajo, Javier Ahumada y Celeste Parisi, especialmente al equipo de trabajo de Javier por habernos otrogado los datos, siendo estos las curvas de luz de las estrellas, el CMD y las imágenes del cúmulo, los cuales fueron usados para este trabajo, además de agradecer al staff de *PyAstronomy* dado que gran parte de los resultados obtenidos en este trabajo fueron hecho con su software, además de responder mis dudas respecto a cómo funcionaban algunos de sus módulos.

UNIVERSIDAD DE CONCEPCIÓN

Abstract

Facultad de Ciencias Físicas y Matemáticas
Departmento de Astronomía

BSc. in Astronomy

A relationship between iron spread and variability in giant stars of globular clusters

by Álvaro LLANCAQUEO

The work presented here is the results from an analysis of 34 light curves, 17 in the V filter and 17 in the I filter of 17 giant stars of NGC 3201, spanning 4 nights of observation carried out on March 20-23, 2013.

The objective of this work was to check and prove if there is a relationship between the variability of a giant star and its iron abundance. To analyze the light curves the Generalized Lomb-Scargle periodogram and the Phase Dispersion Minimization method were computed, and used in order to check if each giant was a variable star. Then a revision of the [Fe/H] values of each variable star from the literature was carried out.

From the period analysis made in the sample of 17 stars, 8 were non-variable, 3 were considered as possible variables and 6 stars were variable. From the sample of the discovered variable stars, they displayed different periods ranging from 0.0881 ± 0.0001 to 0.5418 ± 0.0027 days. These 6 variable stars showed distinct values of [Fe I/H], the 3 most metal-rich stars being RGB, one star with [Fe I/H] $= -1.37$ and two with [Fe I/H] $= -1.31$ dex. The two most metal-poor variables have [Fe I/H] $= -1.61$ and [Fe I/H] $= -1.62$ dex and are AGB stars and one variable showed [Fe I/H] $= -1.50$ dex also being an AGB star. Meanwhile stars that were non-variables showed $-1.56 \leq$ [Fe I/H] ≤ -1.40.

The conclusion brought from this work is that there is a relationship between the iron abundance and variability of giant stars, where stars that are variable present extreme values [Fe/H] compared with the stars that are non-variable and that variability affects somehow the spectroscopic determination of the iron content of giant stars in globular clusters.

UNIVERSIDAD DE CONCEPCIÓN

Resumen

Facultad de Ciencias Físicas y Matemáticas
Departmento de Astronomía

BSc. in Astronomy

A relationship between iron spread and variability in giant stars of globular clusters

by Álvaro LLANCAQUEO

El trabajo presentado es el resultado del análisis de 34 curvas de luz, 17 en el filtro V y 17 en el filtro I de 17 estrellas gigantes de NGC 3201, cubriendo 4 noches de observación realizadas en Marzo 20-23, 2013.

El objetivo de este trabajo fue checkear y probar si hay una relación entre la variabilidad de una estrella y su abundancia de hierro. Para analizar las curvas de luz se utilizaron los métodos "Generalized Lomb-Scargle periodogram" y "Phase Dispersion Minimization", con el fin de ver si cada estrella gigante era una variable. Luego, se realizó una revisión de los valores de [Fe/H] de cada estrella variable en la literatura.

Del análisis de período realizado en la muestra de 17 estrellas, 8 eran no variables, 3 fueron consideradas como posibles variables y 6 estrellas eran variables. De la muestra de estrellas variables descubiertas, mostraban diferentes períodos que van desde los $0{,}0881 \pm 0{,}0001$ hasta los $0{,}5418 \pm 0{,}0027$ días. Además, estas 6 estrellas variables mostraban valores de [Fe I/H] distintivos, las 3 estrellas más "metal-rich" eran RGB, una de ellas con [Fe I/H] $= -1{,}37$ y dos con [Fe I/H] $= -1{,}31$ dex. Las dos variables más "metal-poor" tienen [Fe I/H] $= -1{,}61$ y [Fe I/H] $= -1{,}62$ dex y son estrellas AGB y una variable mostraba un [Fe I/H] $= -1{,}50$ dex siendo también una estrella AGB. Mientras tanto, las estrellas que no son variables mostraban $-1{,}56 \leq$ [Fe I/H] $\leq -1{,}40$.

La conclusión que se obtuvo de este trabajo es que sí hay una relación entre la abundancia de hierro y la variabilidad de las estrellas gigantes, en donde las estrellas que son variables presentan valores extremos de [Fe/H] comparado con aquellas estrellas que no lo son, además que la variabilidad afecta de alguna manera la determinación espectroscópica del contenido de hierro en estrellas gigantes en cúmulos globulares

Contents

List of Figures

List of Tables

Dedicado a todos los miembros de mi familia, a mis padres Álvaro Llancaqueo Valeri y Edith Albornoz Rojas, mis hermanos Javiera Llancaqueo Albornoz and Pedro Llancaqueo Albornoz, y también quiero dedicar este trabajo a mi gata Isis.

Chapter 1

Introduction and Context

1.1. Overview of Globuar Clusters

A Globular Cluster (GC) is defined as a large association of gravitationally bound stars, with diameters between $20 - 100$ parsecs approximately with typically 10^4-10^6 members packed in a (more or less) spherical distribution like a globe, hence the name *globular*. These stellar objects are also known for being the best examples of the oldest objects in the Universe because their stars are mostly low-mass stars and with ages typically greater than 8 gigayears (Gyr). In the Milky Way, as of 2010 there are more than 150 registered GCs (Harris, 1996, 2010 edition), with many of them located in the Halo of our Galaxy, and with recent long-scale surveys in the near- and mid-infrared wavelengths such as the VISTA *Variables in Vía Láctea* (VVV) (Minniti et al., 2010; Saito et al., 2012) increasing even more the amount of (candidate) GCs, with many of them located in the direction of the center of the galactic plane and bulge, which is still a not so well studied region due to the high extinction from interstellar dust.

They have been one of the most influential objects to study since last century, since they have helped us to understand complex processes like stellar evolution and populations, stellar dynamics, galactic nucleosynthesis among others.

Summarizing, the importance of globular clusters in general is that they allow us to check models of stellar evolution and the ages of stars through the use of the Color-Magnitude Diagram (CMD), isochrone fitting, etc. and thus, if we can understand the properties of globular cluster since they are 'complex' systems and, more importantly, their formation history, we can understand how even more complex systems like how our own Galaxy, the Milky Way formed.

Before we talk about more specific characteristics of globular clusters, we need to understand some concepts such as stellar evolution and metallicity, and how we can study such process.

1.2. Stellar Evolution

The processes that all stars passes by that make them change over time is called Stellar Evolution. All stars, without exception, are born in the same way but over time they may differ on how they evolve, such difference in how they evolve depends on their total mass when they reach the main sequence.

1.2.1. The Hertzsprung-Russell Diagram

One of the most important tool to study and understand stellar evolution is the Hertzsprung-Russell Diagram, or H-R Diagram for short. The H-R Diagram is a scatter plot developed by Ejnar Hertzsprung and Henry Norris Russell in 1910 that plots the luminosity L of a star with its surface temperature T_{eff}, with L given by

$$L = 4\pi d^2 f_{bol} = 4\pi R^2 \sigma T_{eff}^4, \tag{1.1}$$

with f_{bol} being the bolometric flux integrated over all wavelengths and corrected for attenuation by the interstellar medium and Earth's atmosphere, d the distance between the star and Earth, $\sigma = 5.67\text{x}10^{-5}$ (erg cm^{-2}K^{-4}) the Stefan-Boltzmann constant, and R the radius of the star.

Since the only way to observe stars (to date) is by collecting photons that they emit, the H-R diagram is natural procedure to organize the information collected from stars and study them. As one can see from Figure 1.1 which shows a complete example of a H-R Diagram, in general there are four distinct groups that can be identified in the diagram:

- The **Main Sequence (MS)**, which is a diagonal band of stars, spanning from blue (brighter) stars to red (fainter) stars. All stars located in this group are those which are burning hydrogen to make helium.
- The **Giant** stars, located above and to the right of the main sequence, meaning that they are brighter than stars from the MS of the same spectral type (or temperature).
- The **Supergiants**, displayed as a more or less horizontal strip consisting of extremely bright stars spanning a huge range of colors from blue (hotter stars) to red (cooler stars).
- The **White Dwarfs**, consisting of a group of extremely faint and mostly blue stars.

The Color-Magnitude Diagram

The Color-Magnitude Diagram (or CMD) is a variant of the H-R Diagram, where instead of plotting the luminosity against the temperature of a star (or their spectral

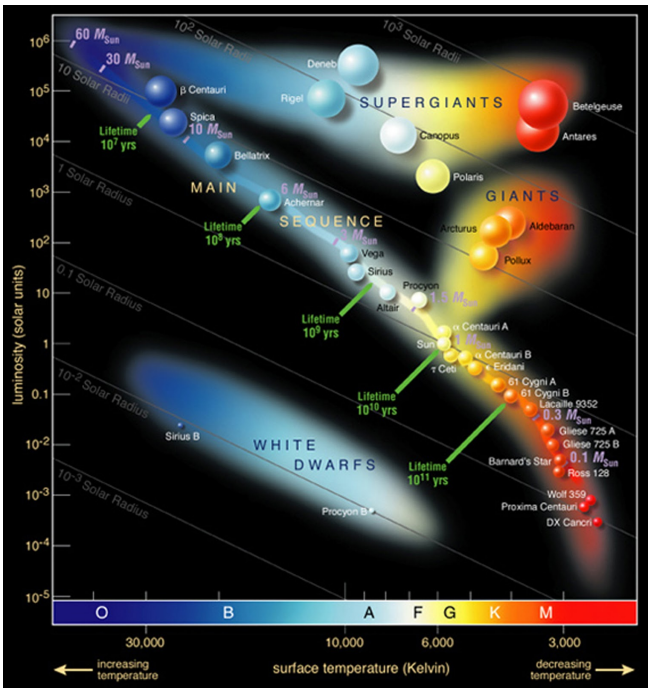

FIGURE 1.1: Example of a Hertzsprung-Russell Diagram displaying the most prominent groups of stars plotting luminosity (in units of solar masses $M_{\odot}$) against surface temperature (in Kelvin). The diagonal lines denotes where stars of equal radii lie in the diagram. Credits: ESO

type), it plots the **magnitude** (which is the brightness) of a star against their **color**. The fact that we can use the color as a measure of temperature comes from the basis that stars can be considered as black-body sources, which enables the use of Wien's Law, defined as

$$\lambda_{max} T_{max} = 2.898 \times 10^{-3} \text{ [mK]} \tag{1.2}$$

with λ_{max} being the wavelength.

In astronomy, a **magnitude** refers to the brightness of a star in a defined filter (or passband). The use of (stellar) magnitudes dates from the ancient Greeks over 2000 years ago with Hipparchus and Ptolemy, where they 'measured´ the brightness of the stars with just the naked eye, to 1850 with Norman Robert Pogson proposing the scale system that is currently used to this day. As previously stated, magnitude measures the brightness of a star that passes through a filter, there are two main types of magnitudes, apparent and absolute magnitude.

Apparent magnitude measures the *flux* f (in ergs^{-1})that pass through a filter of a certain wavelength λ

$$m_{\lambda} = -2.5 \times \log\left(\frac{f_{\lambda}}{f_0}\right) \tag{1.3}$$

with f_0 being a normalized flux which depends on the filter used and it is based on the brightness of the standard star Vega. The normalization values of f_0 are chosen so that the magnitude of Vega is zero.

The **absolute magnitude**, denoted my M_{λ}, is the apparent magnitude that a star

would have if it was located at a distance of 10 parsecs (pc). It is related to the *luminosity* L of the star

$$M_\lambda = m_\lambda - 5\log\left(\frac{d}{10}\right) \tag{1.4}$$

and Eq. 1.4 can be rearranged in order to obtain the quantity known as *distance modulus*.

$$m_\lambda - M_\lambda = 5(\log d - 1) \tag{1.5}$$

The term **color** is defined as the ratio between the flux in two wavelengths expressed as the difference in magnitudes, measured from the brightness of a star between two filters. One thing to note is that magnitudes and colors are defined in such way that lower (or more negative) values of magnitudes mean that the star is brighter or more luminous and in the case of colors more negative or positive means bluer or redder, respectively.

The CMD, in contrast with the H-R Diagram, is mainly used when studying star clusters because all stars are located at the same distance. Figure 1.2 shows the CMD of the globular cluster M3 displaying the different regions that can be found to distinguish the various stellar evolutionary phases of a star, the image was taken from Lamers and Levesque (2017) using data from Renzini and Fusi Pecci (1988).

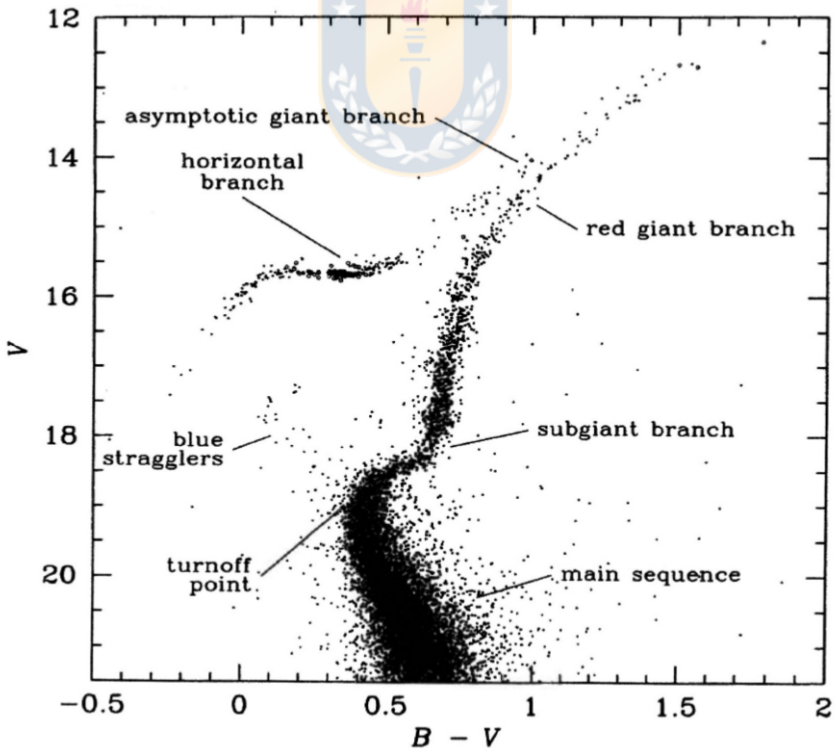

FIGURE 1.2: Color-Magnitude Diagram of M3 showing the nomenclature of the different regions that can be found in it. Credits: Lamers and Levesque (2017) and Renzini and Fusi Pecci (1988).

1.2.2. The Formation of a Star

Stars are formed from a giant (with masses ranging between $10^5 - 10^6 M_\odot$), cool ($10\ K < T < 100\ K$) and dense (with $\rho \sim 10 - 10^2$ particles/cm^3) interstellar molecular gas cloud that becomes unstable to gravitational collapse and compresses itself. From this collapse, the molecular cloud fragments itself into smaller clouds called *clumps*, which start heating up due to the release of gravitational potential energy and reaches hydrostatic equilibrium. These structures collapse and increase their central temperature through the virial theorem (which will be explained in later sections) since nuclear reactions are not effective yet due to the low temperatures, until hydrogen fusion becomes. The structure that is formed from this collapse and heating up, which will later become the nucleus of the forming stars, are called **protostars**.

These newly formed protostars start growing by accretion of the gas and dust from the molecular cloud where they become a *pre-main sequence star* until they reach their final mass. These objects can become a main sequence star if they reach a minimum mass $M_{min} \geq 0.08 M_\odot$ since the temperatures in the nucleus are sufficient to begin nuclear reactions, but there is also an upper theoretical limit to the mass a star (or an accretion disk) can have, called the Eddington limit.

1.2.3. Hydrostatic Equilibrium of Stars

An important condition present in stars is that they are in Hydrostatic Equilibrium, which means that no part of the star is neither contracting (by gravitational collapse) nor expanding (due to radiation pressure), meaning that the inward-directed force from gravity is counterbalanced by and equal outward-directed force from the pressure gradient, which allows to simplify the computation of stellar evolution models.

To determine the equation for hydrostatic equilibrium we begin from the equation of motion, considering a spherical gas system of radius r with mass m_r and density $\rho(r)$. The condition that needs to be satisfied in order to have equilibrium is that the net force is zero. The equation of motion for a unit of volume of a gas with density ρ in the shell at a distance r and with a thickness dr can be expressed as

$$\rho \frac{d^2 r}{dt^2} = -\rho \frac{G m_r}{r^2} - \frac{dP}{dr}, \tag{1.6}$$

with P being pressure and G Newton's gravitational constant. The left side of Eq. 1.6 represents the radial acceleration, the first term of the right side of the same equation is the gravitational force and the second term is the force due to pressure gradient. Since the system is in equilibrium, the acceleration is zero and thus

$$\frac{dP}{dr} = -\rho \frac{G m_r}{r^2}, \tag{1.7}$$

which corresponds to the equation of hydrostatic equilibrium of a star. Figure 1.3 shows an illustrated representation of the hydrostatic equilibrium. Eq. 1.7 can also be rewritten by using the continuity of mass

$$\frac{dm_r}{dr} = 4\pi r^2 \rho \tag{1.8}$$

which results in the following expression

$$\frac{dP}{dm_r} = -\frac{Gm_r}{4\pi r^4} \tag{1.9}$$

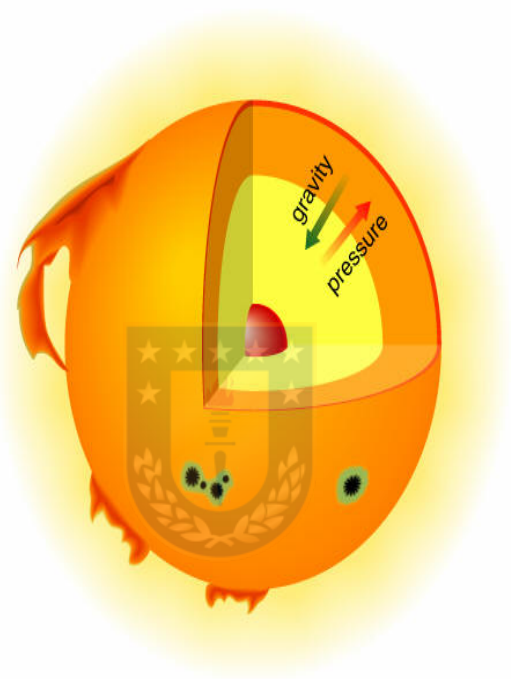

FIGURE 1.3: Illustration of the condition for the hydrostatic equilibrium, denoting that the pressure gradient is equal to the gravitational force. Source: https://people.highline.edu/iglozman/classes/astronotes/stellarevolution.htm

1.2.4. Virial Theorem for Stellar Evolution Theory

In stellar evolution theory, a fundamental theorem that has to be considered is the *virial theorem*, due to the fundamental role that it plays. It relates the total kinetic energy of a self-gravitating body due to the motions of its constituent parts, K to the gravitational potential energy, U of the body.

Consider a bound spherical gas system of mass M in hydrostatic equilibrium, which can be described by Eq. 1.9. By multiplying this equation by $4\pi r^3 dm$ and integrating over dm from the center 0 to the surface of the sphere M on both sides of

the equation, we have

$$\int_0^M \frac{dP}{dm_r} 4\pi r^3 dm = \int_0^M \frac{-Gm_R}{r} dm \tag{1.10}$$

Then, on the left side of the equation we integrate by parts, resulting in

$$\left[4\pi^3 P\right]_0^M - \int_0^M \frac{12\pi r^2 dr}{dm_r} P dm = \int_0^M \frac{-Gm_R}{r} dm \tag{1.11}$$

By using the fact that at the core $r = 0$ and at the surface $P \approx 0$ and due to continuity of the mass (see Eq. 1.8), Eq. 1.11 turns into

$$3\int_0^M \frac{P}{\rho} dm = \int_0^M \frac{Gm_R}{r} dm \tag{1.12}$$

We can note that the right-hand side of Eq. 1.12 is $-U$ and the left-hand side is related to the thermodynamic of the system. By assuming that the system consist of a perfect mono-atomic gas the internal energy per unit mass K can be written as $(3/2)\frac{P}{\rho}$, therefore Eq. 1.12 can be rewritten as

$$K = -\frac{U}{2} \tag{1.13}$$

Eq. 1.13 represent the virial theorem. Since the total energy E_t is defined as

$$E_t = K + U \Rightarrow E_t = -K \tag{1.14}$$

which is negative, in agreement with the hypothesis that the system is bound.

The virial theorem provides some consequences for contracting stars

1. If a star is formed from a very cold contracting extended interstellar cloud with a very small total energy E_t, it must have lost half of its final potential energy in the form of radiation.

2. When a star starts contracting and U decreases, as seen from Eq.1.13 then only half of the released energy is in the form of thermal energy for heating the star, while the other half must be radiated away.

3. When a star runs out of nuclear energy (e.g. depletes its hydrogen) and starts compensating for its radiative energy loss by contracting itself, it must release twice as much potential energy as it radiates because half of the released potential energy is used for heating the star. This means that a contracting star must radiate and increase its temperature, thus moving from its initial position in the HR-Diagram.

Although all stars are born in the same manner from a molecular cloud as protostars, they differ greatly in how they will evolve after being formed. The fundamental parameter of a star that defines how it will evolve during its lifetime and

how long will its lifespan be is its mass when it reaches the main sequence of the HR-Diagram, known as zero-age main sequence (ZAMS) and begin their H-burning stage. The main sequence is the stage were stars spend the majority of their life by fusing H into He. How long the MS (of H-core burnig stage) lasts is given by

$$\tau(H) \sim M^{-2.8} \tag{1.15}$$

A simple explanation of why its lifetime depends on how massive a star is because of *how fast* and *how much* nuclear fuel (hydrogen) it can burn, or fuse into helium. This is because the fusion rate and energy production depends strongly on the star's core temperature. For example, the fusion from H to He via the proton-proton (pp-)chain has a dependence of temperature by T^4.

Table 1.1 summarizes the representative lifetime of a star depending on its mass.

TABLE 1.1: Representative lifetimes of stars as a function of their masses and their corresponding spectral type. Adapted from *Nuclei in the Cosmos* (Bertulani, 2013)

Mass ($M_\odot$)	Time (in 10^6 years)	Spectral Type
60	3	O3
30	11	O7
10	32	B4
3	370	A5
1.5	3000	F5
1	10000	G2 (our Sun)
0.1	1x10^6	M7

1.3. Post-Main Sequence Stars

When a star depletes its hydrogen content in its core by the end of their main sequence life-time, all that remains is an almost isothermal helium (He) core (along with a very small amount of heavy elements) that does not provide energy, because the temperatures at that moment are too low for He burning, along with an hydrogen envelope/shell. Since there is no more radiative pressure, the virial theory does not apply and the gravitational force begins contracting the core of the star along with its layers. From this contraction, the temperature of the star increases up to $T > 10^7$ K in order to perform H-fusion.

How the star will evolve after leaving the main sequence greatly depends on the He-core mass of the star, which can be divided in three groups:

1. Stars with M $< 2M_\odot$ are regarded as **low-mass stars**. These stars develop a degenerate He-core after the MS. Such core leads to a relatively long-lived ***red giant branch*** (RGB) phase. The ignition of He is unstable and occurs in a stage called the ***helium flash*** (Section 1.3.2). By the end of their evolution,

these stars shed their envelopes through stellar winds and their remnants are Carbon-Oxygen (CO) white dwarfs.

2. Stars that have masses between $2 - 8M_{\odot}$ are regarded as **intermediate-mass stars**. They develop a He-core that remains non-degenerate, and they ignite helium in a stable manner. After the central He burning phase they form a carbon-oxygen core that becomes degenerate. As in the case of low-mass stars they also shed their envelopes through stellar winds at the end of their evolution.

3. Stars with $M \approx 8M_{\odot}$ and above are **high-mass stars**. These stars ignite carbon in a non-degenerate core. They also ignite heavier elements in the core until a they form a heavy Fe core, which then collapses, with the exception of stars with masses in the range of $\approx 8 - 11M_{\odot}$.

An important parameter at the end of the MS is the *Schönberg-Chandrasekhar limit* (SC-limit) given by $(M_{\rm core}/M_{\rm total}) = 0.37\,(\mu_{\rm env}/\mu_{\rm core})^2$, with μ being the molecular weight, which corresponds to the maximum mass that the core can reach. Depending on the value of the ratio the core can contract or remain in equilibrium. If $(M_{\rm core}/M_{\rm total}) < 0.1$ the core remains in hydrostatic equilibrium, but if $(M_{\rm core}/M_{\rm total}) > 0.1$ then the core will contract. A star's evolution after leaving the MS also depends on its metallicity.

Furthermore, an important effect that occurs during the core contraction is the **mirror action** of the core, which consist on the following principle principle: Whenever a star has an active shell-burning source, the burning shell acts as a mirror between the core and the envelope. This means that if the core contracts, the envelope expands and vice-versa. Such action can be understood with the following explanation: In order to maintain thermal equilibrium, the burning shell must remain at a constant temperature due to the thermostatic action of nuclear burning.

1.3.1. Red Giant Branch

Red giant stars are the results of stars from their core contraction after they burned almost all their H in their core. As explained before, as a red giant stars they evolve differently depending on their mass. A good way to present the evolution of stars is to use a combination of the H-R Diagram of the star along with the ***Kippenhahn diagram*** (Kippenhahn, 1965), such diagram which describes the changes in the interior stellar structure as a function of time and mass fraction (x- and y-axis respectively) which is presented in Figure 1.4, the phase between points A and B correspond to the main sequence H-fusing phase.

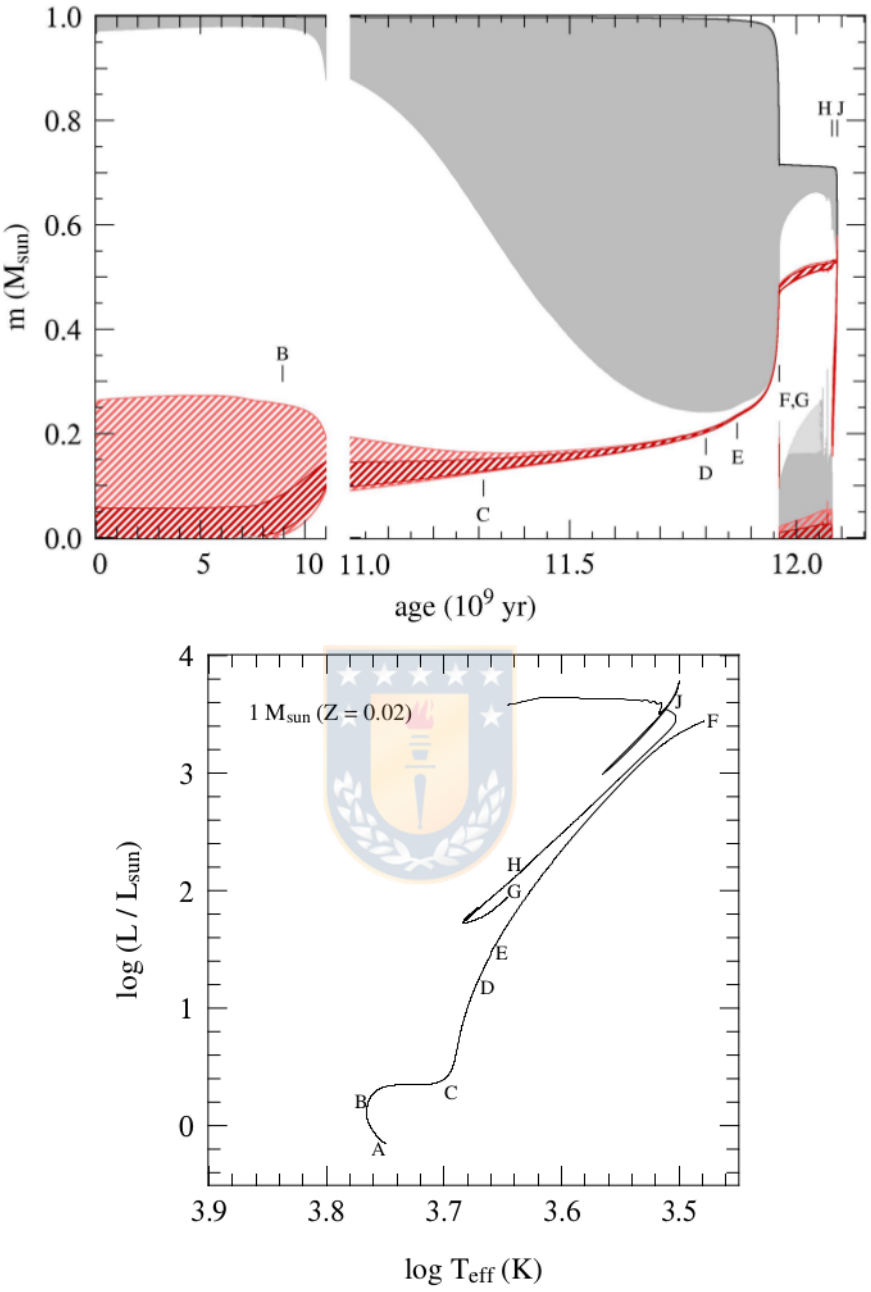

FIGURE 1.4: Combination of Kippenhahn diagram (top panel) and the H-R Diagram (bottom panel) presenting the evolution of a star of $1M_{\odot}$. Red areas indicate fusion regions: darker areas are for efficient fusion and lighter areas inefficient fusion. Gray regions indicate convection, while the light gray area indicates semi-convection. Credit to the lecture notes of Stellar Structure and Evolution by Onno Pols, 2011: http://www.astro.ru.nl/~onnop/education/stev_utrecht_notes/.

Low-mass star evolution

For the evolution of low-mass stars it is necessary to remember that these stars do not have a convective core during their main sequence phase. The evolution of these kind of stars will be explained with the use of Figure 1.4 as reference of the different phases.

At the phase B-C, which is known as the ***sub-giant branch*** the H from the core is depleted and the core stars to contract, increasing T, and H begins fusing at the shell around the core. The H-shell fusion occurs via the CNO cycle, the core contracts at a very slow pace and the envelope expands due to the mirror action, and from this expansion the outer layers starts to cool and the envelope opacity increases and becomes convective. This phase lasts $\sim$ 2 Gyr. At point C, the He-core becomes degenerate because of the contraction, almost half of the stellar mass is convective and the star reaches the *Hayashi line*, located at $T \sim 3500$ K. From this point onward the star is regarded as a **red giant**.

After becoming a *red giant* (phases C-D) the H-shell fusion continues to add mass to the core, contracting it, and due to the mirror action, the shell expands. Since the star is on the *Hayashi line* its T_{eff} is mostly constant, meaning that the expansion of the star leads to an increase of luminosity and stars climbing the Hayashi line in the H-R Diagram. As the core contracts, the density in the shell increases since it is directly on top of the core, making the shell-fusion more efficient and in turn producing the required luminosity for equilibrium. Such phase lasts $\sim$ 0.5 Gyr. At point D, the surface abundance may now start to show evidence of a slight He enrichment, along with a slight increase in the N abundance, and a slight decrease of C and O. This is known as the *first dredge up*.

At phases D-E-F the core keeps growing in mass and shrinking, leading to a continuous expansion and increase in luminosity. with the H-shell fusion reaching hotter layers, becoming more efficient and producing the required luminosity, which can be seen clearly in the top panel of Figure 1.4. The RGB phase ends at phase F, when the He-core reaches a mass $M_{core} \approx 0.45 M_{\odot}$. The contraction lead to an increase of temperature high enough to begin the He-core fusion, which will be explained in Section 1.3.2.

Intermediate and high-mass star evolution

For the case of stars with intermediate masses their evolution is similar as in the case for low-mass stars, with their tracks in the H-R Diagram having the same structure as in Figure 1.4, going through the subgiant and red giant phases (as in phases B-C and D-E-F) when the star is convective and evolves upward on the Hayashi track. But there are a few notable differences.

1. The He-core is at first smaller than the SC-limit. Due to this the core remains in equilibrium and does not contract. But due to the H-shell fusion, which creates

He that adds to the core, it does later exceed the SC-limit and contract.The star expands due to the mirror action and the depth of the convective envelope increases, like in the case of low-mass stars.

2. The He-core does not become degenerate during the H-shell fusion, which can be explained due to their high temperatures T and low densities (ρ) at the start of this process. Furthermore, the H-shell fusion ends when the He-core mass reaches a slightly higher value than $M_{core} \approx 0.5 M_{\odot}$ for low-mass stars.

3. The evolution timescales is much shorter that in the case of low-mass stars. For example, the times to cross the H-R Diagram from the end of the MS up to the Hayashi line (phases B to C from Figure 1.4) for a star of $1 M_{\odot}$ and $5 M_{\odot}$ are approximately 2.3 Gyr and 2.4 Myr, respectively.

1.3.2. Horizontal Branch

When a star reaches the tip of the RGB ($L \sim 10^3 L_{\odot}$, as seen in point F of Figure 1.4), the He-core reaches enough temperature ($T_{core} \sim 10^8$ K) to ignite the Helium in the core, such provides an increase of T, with such rise depending if the He-core is *degenerate* or not, with such degeneracy depending on the initial mass of the star M_i. For the case of a *degenerate* core (stars with $M_i \leq 2 M_{\odot}$) the He-core fusion is *explosive* (known as the **Helium Flash**). Meanwhile, for stars with *non-degenerate* cores (stars with $M_i > 2 M_{\odot}$) the He-core fusion (and T increase) is done gradually. From this, the star has two sources of energy, the core that is fusing He into carbon (C), with C combining with He to make oxygen (O), and the shell providing H-shell fusion around the core. The star becomes less luminous and hotter and moves in a zone of the CMD known as the Horizontal Branch, which can be located at phases F-G-H from Figure 1.4.

1.3.3. Asymptotic Giant Branch

The Asymptotic Giant Branch (AGB) is the stage that intermediate- and low-mass stars reach after finishing their core He-burning phase at the end of the Horizontal Branch, where all that remains is a Carbon-Oxygen core (CO core) along with a He- and H- burning shells. The AGB is one of the most interesting phases of stellar evolution due to various characteristics that stars in this phase present. It corresponds to the phases H-J from Figure 1.4.

The composition of an AGB star is from the most external region to the inner parts of the star as it follows (see Figure 1.5 shows an illustrated example):

- A convective H-rich envelope
- An H-burning shell, producing He
- A He-rich intershell zone

- An He-burning shell, fusing He to C and subsequently C to O
- A degenerate CO core

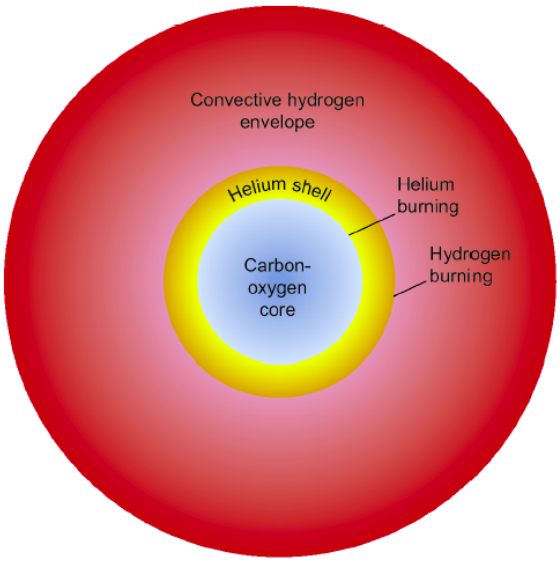

FIGURE 1.5: Illustrated structure of an AGB star. Source: http://www.astro.uvic.ca/~fherwig/sevol.html

As in previous phases, the core (now composed of C and O) temperature is too low for nuclear reactions, meaning that it does not provide energy and it starts to contract. Due to the H-burning shell, the core contraction results in an expansion of the envelope, which translates in a shift to the right in the HR diagram and subsequent slight loss of luminosity. The core contracts until the He begins to ignite in a shell just above the CO core.

Since the He-burning shell is immediately above the CO core, the pressure in the shell and its energy production are mainly set by the mass of the core, which is similar to what occurs in RGB stars from Section 1.3.1. After the He-shell fusion begins, the H-shell fusion switches off, because the He shell begins to expand, which in turn makes that the outer layers begin to expand as well. This expansion of the H-shell decreases the temperature T and density ρ, thus almost stopping the H-shell fusion (in case of low-mass stars $M_i \leq 4M_\odot$ the H-shell fusion is still active but at a low level).

With both He-shell and H-shell fusions active, the mass of the core increases which in turn increases the luminosity, but with a constant T_{eff}, implying an increase of the star's radius. This increase of radius is achieved by deepening the convection zone of the star, meaning that the convective zone stars penetrating inwards, into the H-depleted zone. If the convective zone reaches the He-rich intershell zone, it mixes the products of H-fusion (CNO cycle) into the outer envelope and those products are brought to the surface through convection. This process is known as the *second*

dredge up. Furthermore, this process does not occur in low-mass AGB stars due to the still active H-shell fusion.

Another interesting process that happens during the AGB phase, especifically when the star is starting to climb the *Hayashi track*, is that the two shell-burning phases alternate in producing the energy for the star in intervals of $10^3 - 10^5$ years. This process known as the **thermally pulsing phase**.

For more massive stars ($M_i \geq 4M_\odot$) during the later thermal pulsing phase there is a *third dredge-up*, where s-processes elements, along with C are brought to the atmosphere of the star.

Observations of AGB stars show that they all suffer from mass loss by the end of this evolutionary stage, with such mass loss being explained through nuclear fusion inside the star and also due to stellar winds. The AGB phase is terminated by such mass loss, since their envelope is stripped (almost) entirely. Depending on how much mass is lost, it will set up the mass of the resulting white dwarf for low-mass stars or the supernova rate for intermediate and high-mass stars.

1.4. Metallicity

In astronomy, the two most important and most abundant elements in the Universe are Hydrogen (H) and Helium (He), and every other elements beyond He (e.g. Li, C, N, O, Na, Fe, etc.) are referred as *metals*, which is different from the conventional definition of metals in chemistry; simply put, metals are defined 'all elements except H and He´. In a star, nebula or even in a galaxy, we can find a portion of the materials that is made up of these elements besides H and He.

There are different methods that can be used to describe and measure the abundances of metals in stars or other celestial bodies. The most common methods are the following:

1.4.1. Determining stellar composition using mass fraction

To determine the fraction of elements that are in a star (especially our Sun), H, He and all metal are denoted as X, Y and Z respectively, each referred as 'mass fraction´ with each quantity defined so that

$$X + Y + Z = 1.0 \tag{1.16}$$

where

$$X \equiv \frac{m_{\mathrm{H}}}{M}, \tag{1.17}$$

$$Y \equiv \frac{m_{\mathrm{He}}}{M}, \tag{1.18}$$

$$Z \equiv \sum_{i>\mathrm{He}} \frac{m_i}{M} = 1 - X - Y, \tag{1.19}$$

with $m_{\rm H}$, $m_{\rm He}$, m_i being the fractional mass of H, He or any element heavier than He (i) that the star contains, respectively and M being the total mass of the system.

1.4.2. Determination of chemical abundance ratios

Metallicity, or chemical abundance ratio, consist of a measurement of the abundance of metals, even though the most abundant elements among metals include C, N, O, Ne, Si, Mg, Al, Na, etc. with the most prominent heavy element in stellar spectra being Iron (Fe), it is defined as

$$[\mathrm{Fe/H}] = \log_{10}\left(\frac{N_{\rm Fe}}{N_{\rm H}}\right)_{\rm Star} - \log_{10}\left(\frac{N_{\rm Fe}}{N_{\rm H}}\right)_{\rm Sun} \tag{1.20}$$

where $N_{\rm Fe}$ and $N_{\rm H}$ are the number of iron and hydrogen atoms per unit of volume respectively. As seen in eq. 1.20, the abundance ratio is defined as the logarithm of the ratio of a star's iron abundance compared to that of the Sun. For example, a star that display an $[\mathrm{Fe/H}] = 0$ means that it has the same iron abundance as the Sun; whereas if a star has an $[\mathrm{Fe/H}] = -1$ it has one tenth or 10^{-1} of Iron abundance compared with the solar value, with

$$\log_{10}\left(\frac{N_{\rm Fe}}{N_{\rm H}}\right)_{\rm Sun} = -4.5\ [\mathrm{dex}]$$

detailed in Martin Asplund et al. (2009).

The measurements of chemical abundances for stars, especially for a large group such as in a stellar cluster, are fundamental to understand the formation history of such stars, and in fact it does since the presence of heavy elements comes from the nucleosynthesis occurring in the core of a star as it evolves.

As stars evolve they release metals through stellar winds or (if they are massive enough) they explode in the form on a supernova ejecting heavy elements into the interstellar medium (ISM), enriching it. Stars that are formed later from this metal-enhanced ISM will present in their stellar atmospheres the spectrum of these elements.

1.5. Chemical characteristics of Globular Clusters

With the concept of metallicity already explained, it is possible to understand specific characteristics of globular clusters such as their chemistry. At first, from a chemical perspective GCs were first thought to be an example of simple stellar population (SSP) due to the assumption that all globular cluster members (their stars) tend to have the same chemical content, making astronomers think that they GCs are chemically homogeneous. But over the last couple of decades through technological development, spectroscopic observations began to provide more detailed chemical analysis for GCs, showing that almost all GCs display inhomogeneities in their light

element content, such elements are C, N, O, Na, Mg, and Al; explained for example in the *Annual Review* from Gratton, Sneden, and Eugenio Carretta (2004).

A decade ago, Eugenio Carretta along with many collaborators published a series of papers in 2009 (see E. Carretta et al., 2009a; E. Carretta et al., 2009b; E. Carretta et al., 2009c) detailing the chemical analysis of 19 globular cluster by using spectroscopic data from UVES and GIRAFFE, where the results from these papers showed that almost all GCs display inhomogeneities in their light element content with the most prominent feature being the Sodium-Oxygen (Na-O) and Magnesuim-Aluminum (Mg-Al) anticorrelations as seen in Figure 1.6 for the former anticorrelation. Such inhomogeneities provided a new way to define GCs along with the term of ***multiple populations*** giving at least two different populations: the ***first population*** (or first generation) stars which are Na-poor O-rich, similar to halo field stars and the ***second population*** (or second generation) stars that are rich in Na but poor in O. Such results from these studies were fundamentar since they proved that the belief of GCs as examples of SSPs had to be modified. The only known case of a globular cluster that does not exhibit this Na-O anticorrelation is Ruprecht 106 presented in Villanova et al. (2013).

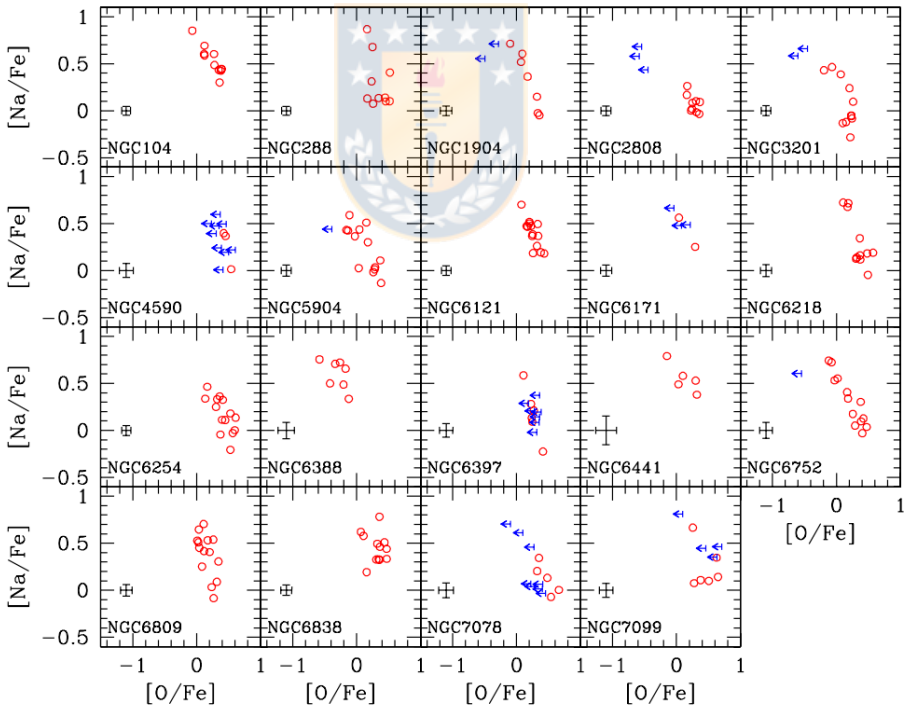

FIGURE 1.6: The Na-O anticorrelation observed in 19 GCs by E. Carretta et al. (2009c) from UVES spectra. The blue arrows indicate the upper limit of O abundances and the detection are indicated as red open circles and the star-to-star variation errorbars are marked in each panel individually. Figure taken from E. Carretta et al. (2009c)

In order for globular clusters to have such defined chemical patterns they must have been chemically enriched during their early stages of formation, meaning that their interstellar medium (ISM) was polluted with such elements allowing multiple

generations of stars to be formed within the GC (Gratton, Sneden, and Eugenio Carretta, 2004) suggesting that GCs have been able to retain low-energy ejecta casued by those polluters. Some of the suggested polluters over the years are: Intermediate-mass asymptotic giant branch (AGB) stars from D'Antona et al. (2002) and D'Antona et al. (2016), fast rotating massive main sequence (MS) stars (e.g. Decressin, Charbonnel, and Meynet, 2007) and massive binaries (de Mink et al., 2010).

1.5.1. The Metallicity Distribution in Globular Clusters

As mentioned previously, GCs were at first regarded as SSPs but such manner of thinking had to be modified due to the findings of star-to-star variation of their light elements, but there was still the fact that chemical analysis in GCs showed negligible internal abundance variations of iron-peak elements (e.g. E. Carretta et al., 2009a), in other words GCs have more-or-less an homogeneous Fe content. But such claim also had to be thought again due to observations of one the most interesting and massive globular cluster ω Centauri, with the results in Geyer (1967) discovering that this cluster had an anomalous width in its giant branch, which was later confirmed by Cannon and Stobie (1973), presenting photoelectric data of more than 120 stars with magnitudes up to $V \sim 16.5$, finding that the giant branch of ω Centauri really displayed a large scatter that was neither due to photometric errors, field stars or differential reddening and remarked the scatter was intrinsic (see Figure 1.7). Two years later, Freeman and Rodgers (1975) investigated the abundances of 25 RR Lyrae stars, finding a large spread in [Ca/H], varying from -1.6 to -0.4 dex.

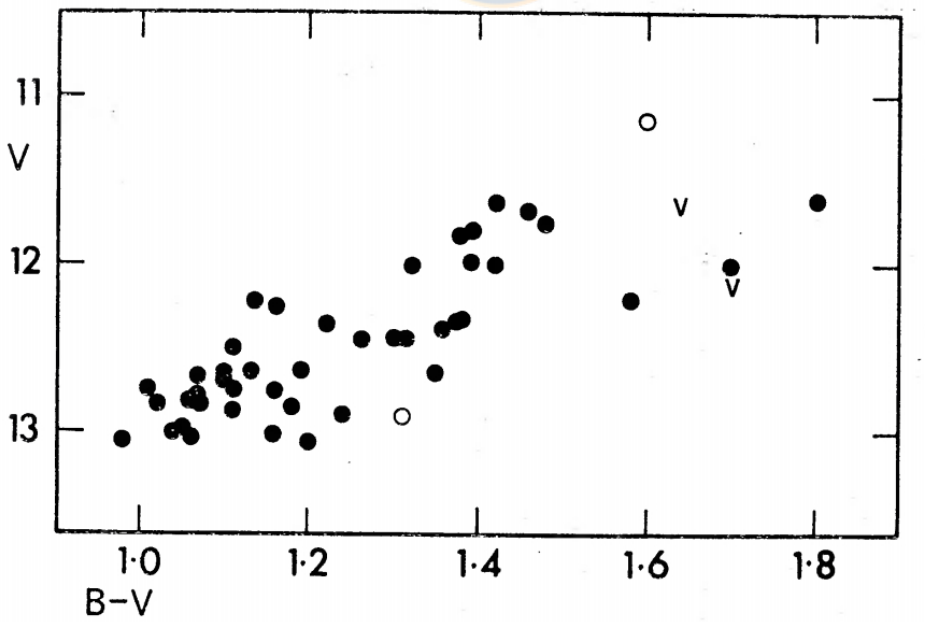

FIGURE 1.7: The CMD of ω Centauri displaying an anomalous width of its giant branch. Credits: Cannon and Stobie (1973)

With further investigations regarding the abundances of ω Centauri (e.g. Livia Origlia et al., 2003; Pancino et al., 2011; Marino et al., 2011a) over time, the results

from such works showed that this massive GC displays a multi-modal metallicity distribution, which spans a range of $\sim$ 1 dex.

But ω Centauri was not the only GC that displayed this feature. Another well studied massive GC, Terzan 5 located at the bulge of the Milky Way also displayed a multi-modal distribution as shown for example, in L. Origlia et al. (2011) and L. Origlia et al. (2013), spanning a range of $\sim$ 1 dex. A third case, which is a GC located in the central region of the Sagittarius dwarf spheroidal galaxy, M54 also showing a spread (e.g. Bellazzini et al., 2008; A. Mucciarelli et al., 2017), although its metallicity distribution is not as large as ω Centauri and Terzan 5, due to the contamination of the Sagittarius stars which enhance such distribution.

Although, these clusters have this feature in common, they do not have the same (possible) explanation for such distribution. For the case of ω Cen, its metallicity distributon can be explained due to being interpreted as a remnant core of a dwarf spheroidal galaxy (Bekki and Freeman, 2003). In Terzan 5's case Ferraro et al. (2016) discussed the possibility that it could likely be a relic of a primordial structure that contributed in the formation of the Galactic Bulge. Finally for M54, its spread can be explained from its position in the core of the Sagittarius galaxy and due to its distinct dispersion velocity, this cluster should have been formed independently by the *real* nucleus of the galaxy and due to dynamical friction (which was demonstrated by Bellazzini et al., 2008) it decayed to the present-day position.

In recent years, there have been many studies to find other GCs displaying intrinsic iron spread, although with smaller metallicity distribution (typically in the order of $\sim$ 0.1 dex) than the three GCs already mentioned. Examples of such clusters are:

- M22 (Marino et al., 2009)
- NGC 3201 (Gonzalez and Wallerstein, 1998; Simmerer et al., 2013)
- M2 (Yong et al., 2014)
- NGC 5824 (Da Costa, Held, and Saviane, 2014)
- NGC 5286 (Marino et al., 2015)
- M19 (Johnson et al., 2016)

although some of these clusters were re-evaluated later by other studies to either prove their intrinsic spread or conclude that those findings were not correct at all, such studies are A. Mucciarelli et al. (2015b) and A. Mucciarelli et al. (2015a) for NCG 3201 and M22 respectively, Lardo, A. Mucciarelli, and Bastian (2016) for M2 and Alessio Mucciarelli et al., 2018 for NGC 5824.

1.6. Variable Stars

From previous sections, from the different groups of stars that can be found during their lifetime, one of the most interesting groups are the giant stars, those who are near the end of their lives because of all the different processes that happen at these stages. Another kind of stars that are as important as the giant stars are *variable stars*. A variable star is (as it name suggest) a type of star that varies its apparent brightness (magnitude) over time from the perspective of the Earth. Such changes in their magnitudes can be as low as a thousandth of a magnitude to up to as large as in the order of twenty magnitudes, but those magnitude changes can also be fast as in a couple of seconds to really slow a couple of years.

Variable stars can be classified in two groups depending on how their brightness changes. Such groups are:

- **Extrinsic Variables**
- **Intrinsic Variables:** Variables that display brightness change due to intrinsic properties or physical changes of the star such as eruptions or pulsations.

For the case of extrinsic variable stars, there are two classes of variables, **Eclipsing** and **Rotating** variables. The former are a type of variable that are generally found in binary systems, these stars that display changes in their brightness because their orbiting companions (another star) pass in front of each other, thus obscuring the light that reaches the Earth. The later are stars that show small light changes caused by patches of light spots on their surfaces, or dark and bright areas on the surface of the stellar structure that causes small changes on the apparent brightness of the star when the star rotates.

From the group of intrinsic variables, there are also two classes, **Eruptive** and **Pulsating** variables. The eruptive (or cataclysmic) variables are those that display significant or rapid changes in their luminosity due to violent outbursts that are caused by thermonuclear processes either from the surface of from the internal structure of the star. Pulsating variables on the other hand are those who change their brightness due to the periodic expansion and contraction of their surface layers. In most cases these stars pulsate because they are at the end of their lives and have become unstable (e.g. AGB stars). In both classes of intrinsic variables, there are different types of variable stars. For example, types of explosive variables are Supernovae, various types of Novae and Symbiotic stars; whereas for the pulsating variables one can find the well studied Cepheids, RR Lyrae , Long-period variables, etc.

In general, variable stars have a great importance for astronomy since their study allow us to understand and determine the various properties of a star, such as mass, luminosity, radius, temperature, their structure, etc and also understand stellar evolution (for the case of intrinsic variables). Furthermore, since their variability can

either be fast or slow, these objects are challenging because they have to be systematically observed for long time-scales in order to determine their long-time behaviour which is in principle difficult.

1.6.1. Pulsating Stars

Pulsating stars have been, and continue to be important to understand part of the stellar evolution and also are useful in the study of globular clusters. The are many reasons to study these objects, such as the understanding of their luminosity, spectral type, their pulsation cycle and other general properties, which help us understand pulsating stars itself (their structure). Furthermore, they can be classified into groups with homogeneous properties, and from this one can calibrate their absolute magnitudes and use them to derive distances. The most used and studied pulsating stars are the RR Lyrae and Cepheid stars. Due to this pulsating stars have been the basis of not only Galactic and extragalactic distance scales, but also the determination of ages and distance of globular clusters which has been done by comparing theoretical isochrones in CMDs with the ones obtained in observations.

Pulsating Red Giants

From stellar evolution, red giant stars are unstable to radial pulsations; in fact, as stars begin evolving by expanding and cooling themselves to become red giants or AGB stars, they start to become pulsationally unstable, which means that (virtually) every star found in the upper right portion of the H-R diagram is a variable. From this, we can call such objects as pulsating red giants (or PRGs).

Pulsating red giants are complex objects, mainly due to their variability being a mix of pulsation and convection (being a not well understood process in astrophysics), with extended atmospheric envelopes (Catelan and Smith, 2015) and they cannot be ignored, since they are quite numerous among the bright stars. Now a days we are able to make general statements of PRGs:

- Giants that are cooler than those of spectral type K5III tend to be variable in brightness, with such stars making up $\sim$ 10% of the stars in the *Yale Catalogue of Bright Stars*[1].
- The cooler the giant, the longer the period; such periods are consistent with low-order radial pulsations.
- The cooler AND larger the giant, the larger the amplitude of variability; with the large-amplitude *Mira* stars being the most extreme cases
- Pulsating red giants tend to be semi-regular (SR), especially the small-amplitude ones, though there are usually one or more strict periods present. In fact, many small-amplitude stars and large-amplitude SR variables are multiperiodic.

[1] http://tdc-www.harvard.edu/catalogs/bsc5.html

- Up to 50% of the small-amplitude PRGs display long secondary periods, which are typically ten times the primary (radial) period; there is currently no explanation for this long secondary periods, despite the efforts of investigations like Wood, Olivier, and Kawaler (2004).

The classification of pulsating red giants

Over history, the classification of pulsating red giants have been done on the basis of the period, amplitude, and regularity of the light curve. PRGs are classified as the following according to the *General Catalogue fo Variable Stars*[2] (GCVS) (Samus' et al., 2017):

- *Mira variable*: Long-period variables with late-type emission spectra (Me, Ce, Se) and amplitudes ranging from 2.5 - 11 mag in V. They display a well pronounced periodicity, and the periods lie in the range between 80 and 1000 days. Infrared amplitudes are usually less than in the visible and may be <2.5 mag.

- *SRa variables*: Late-type (M, C, S or Me, Ce, Se) giants (Z Aqr). They show persintent periodicity and have amplitudes < 2.5 mag in V. Their periods are in the range of 35-1200 days. Many of these stars differ from Miras just by displaying smaller amplitudes.

- *SRb variables*: Semiregular late-type (M, C, S or Me, Ce, Se) giants that have poorly expressed periodicity, with mean cycles in the range of 20-2300 days, or with alternating intervals of periodic and slow irregular changes, and even with light constancy intervals (RR CrB, AF Cyg).

- *Lb variables*: Slow irregular variables of late spectral types (K, M, C, S), usually CO Cyg giants.

For the cases of red supergiants they can be classified as *SRc variables* for semi-regulars, with yellow SR supergiants as *SRd variables*, and *Lc variables* for the irregulars. Even though these stars are generally well classified, there are a couple things to be noted: The classification between semi-regular and irregular is arbitrary, since it requires a large amount of data and an extreme careful analysis to determine how much periodicity is present in a star. And the difference between *Mira* and *SRs* (an amplitude of 2.5 mag in V) is also arbitrary. Furthermore, Olin Eggen published a series of papers during the 1970's developing a general classification for PRGs: large, medium and small-amplitude red variables (LARV, MARV and SARV, respectively), along with the classification Sigma Librae variables, which consists of stars with amplitudes less than 0.2 in V.

[2] http://www.sai.msu.su/gcvs/gcvs/

Chapter 2

Is there a relationship between variability and iron abundance?

2.1. A metal-poor variable RGB star in NGC 6528

Last year, in the investigation from Muñoz et al. (2018), the authors analyzed the chemical abundances of 7 red giant stars of the bulge globular cluster NGC 6528 using high-resolution spectra from FLAMES@UVES.

From their analysis they provided a peculiar result: They found that one of the RGB stars from their sample was

1. More metal-poor, with an $[\mathrm{Fe/H}] = -0.55$, compared to the other 6 stars that they analyzed (with a mean value of $[\mathrm{Fe/H}] = -0.14 \pm 0.03$). Even though that anomalous star displays the same chemical patterns as the rest of the sample.

2. Using data from the VVV public survey (Minniti et al., 2010; Saito et al., 2012) and analyzing the data with the Generalized Lomb-Scargle (Zechmeister and Kürster, 2009) and Phase Dispersion Minimization (Stellingwerf, 1978) algorithms, they found that this particular RGB was also a variable star with a period of ~ 0.26 days and an amplitude of 0.05 mag in K_s filter.

In light of this finding from this work, the following question arose:

"Could the variability of a star be related with the difference in its iron abundance compared with the rest of the stars that are not variable?"

For this, in order to answer such question the objective of this work was to revisit one of the globular clusters that was questioned for their spurious iron content, in this case NGC 3201.

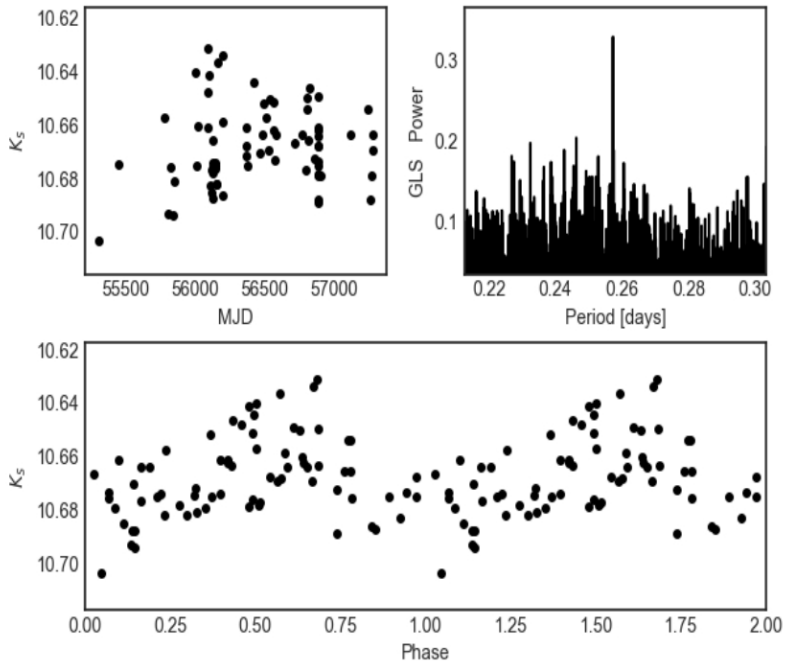

FIGURE 2.1: Top panels: Light curve and result from the Generalized Lomb Scargle periodogram of the metal-poor variable RGB, displaying a strong peak at 0.25729 days. Bottom panel: Phased light curve of the variable RGB star. Credits: Muñoz et al. (2018, Fig. 5)

2.2. Objectives of this investigation

2.2.1. General Objectives

The main objective of this investigation is to study the possible variability of giant stars of a Galactic Globular Cluster in order to test if this phenomenon has a relation with the iron spread in such cluster.

2.2.2. Specific Objectives

The specific objectives of this work are the following:

- Obtain time-series photometric data from giant stars of the previously studied galactic globular cluster NGC 3201.
- Obtain light curves of each of those giant stars.
- Analyze each light curve in order to determine if each giant star is variable or not.
- Identify the Red Giant Branch (RGB) and Asymptotic Giant Branch (AGB) stars of the cluster.
- Search from literature the iron (Fe) abundances of each star.
- Prove if there is a relation between variability of a star and its iron abundance.

Chapter 3

Previous investigations of NGC 3201

3.1. General information of NGC 3201

The Globular Cluster NGC 3201, is a low galactic globular cluster located in the southern constellation of Vela. The main parameters of this cluster which are taken from Harris (1996, 2010 edition) are shown in Table 3.1.

This particular GC has a number of distinct features, such as being nearby ($V_{HB} = 14.76$ mag), an extremelly high radial velocity ($v_r = 494 \mathrm{kms}^{-1}$) and also an orbital velocity of 250km s^{-1} around the Galactic center but in a retrograde sense (Gonzalez and Wallerstein, 1998). Another important feature of NGC 3201 is that it contains a large number of variable stars including RR Lyrae and of Oosterhoff type I ($N_{RR} \approx 80$), and from its CMD (Layden and Sarajedini, 2003) it has a very populated and extended horizontal branch were the authors also reports the finding of variable red giant branch (RGB) stars.

TABLE 3.1: Main parameters of the galactic globular cluster NGC 3201. Right Ascension α and Declination δ values are in J2000. d and R_{GC} are the distances from the Sun and Galactic Center respectively, with the later assuming $R_0 = 8.0$ kpc.

Parameters	Values
α_{2000}	10h 17m 36.82s
δ_{2000}	-46° 24′ 44.9″
l	277°.23
b	8°.64
[Fe/H]	−1.59 dex
V_{HB}	14.76 mag
$E(B-V)$	0.24 mag
d	4.9 kpc
R_{GC}	8.8 kpc

One thing to note about this GC is that, due to its location in the Galactic plane ($l = 277°.28$, $b = +8°.461$) it has a notorious differential reddening ($E(B-V) = 0.24$ mag) (von Braun and Mateo, 2001).

3.2. The dubious intrinsic iron spread of NGC 3201

NGC 3201 has been a controversial cluster in the last couple of decades due to its various spectroscopical studies that analyzed its [Fe/H], being one of the few globular clusters that displayed a metallicity distribution as shown in Section 1.5.1, with different investigations obtaining different results regarding the cluster's metallicity.

For instance, the results from Gonzalez and Wallerstein (1998) using CTIO high-resolution spectra and Simmerer et al. (2013) taking high-resolution spectra from UVES-FLAMES@VLT and MIKE@Magellan, claimed that NGC 3201 is a globular cluster with an iron spread of $\sim$ 0.4 dex (Figure 3.1).

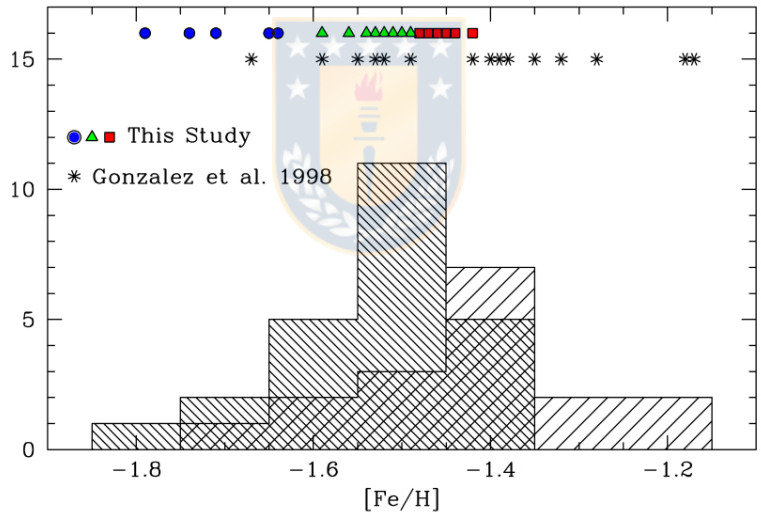

FIGURE 3.1: Distribution of [Fe/H] of the stars studied by Gonzalez and Wallerstein (1998) (light histogram) and Simmerer et al. (2013) (dark histogram). The different points are the ones that the authors used to construct the graph and the different colors (blue, green and red) mark the most metal-poor, intermediate-metallicity and most metal-rich stars, respectively. Credits: Simmerer et al. (2013, Fig. 1).

But other studies like, for example Muñoz, Geisler, and Villanova (2013) using high-resolution, high signal-to-noise ratio spectra from MIKE@Magellan did not find such spread, finding a [Fe/H] $= -1.53 \pm 0.01$ dex. An interesting thing that the authors point out is that 5 out of the 6 most metal-poor stars (with [Fe/H] ≤ -1.59) from Simmerer et al. (2013) might be asymptotic giant branch (AGB) stars instead of red giant branch (RGB) stars.

3.3. Latest results regarding the iron abundance of NGC 3201

Since the investigations made in 2013, there was not a clear statement regarding the iron content of NGC 3201, due to the discrepancies in the results from each investigation such as the ones previously mentioned. It was not until Alessio Mucciarelli an his team in 2015 re-analyzed the spectra of 21 stars from the sample of Simmerer et al. (2013) using high-resolution spectra with UVES-FLAMES@VLT detailed in A. Mucciarelli et al. (2015b) in light of the results from Lapenna et al. (2014).

What was found in Lapenna et al. (2014) is the following: They studied 24 AGB stars in the globular cluster 47 Tucanae and from their investigation they discovered effects due to non-local thermodynamical equilibrium (NLTE). They point out that such NLTE effect affects the abundances that are obtained from Fe I lines, but leave the abundances from Fe II are unaffected. Moreover, they point out that RGB stars do not display such effects and as such, the abundances of Fe I and Fe II match each other.

From this results, the procedure used by authors from A. Mucciarelli et al., 2015b was the following: They measure T_{eff} from the data. But the measurement of $\log g$, in contrast with the T_{eff} is derived by adopting photometric gravities using the Stefan-Boltzmann equation and then measuring Fe I and Fe II lines individually. From their methods they discovered that the spread found in Simmerer et al. (2013) was due to the presence of AGB stars in the sample, finding that while their estimates of the [Fe I/H] ratio are very similar to those from Simmerer et al. (2013), since the Fe II lines are not affected by the NLTE effects in AGB stars, the iron abundance derived from Fe II lines were much smaller, leading to the conclusion that NGC 3201 does not have an intrinsic iron spread (see A. Mucciarelli et al., 2015b).

But one thing to note is that for GCs with metallicity similar to NGC 3201, NLTE corrections models from Maria Bergemann et al. (2012) and Lind, M. Bergemann, and M. Asplund (2012) predicts that the Fe I lines should be affected in a similar way regardless if the star is an RGB or AGB star. Such predictions mean that there could be another mechanism that may explain the behaviour of the iron content of the cluster.

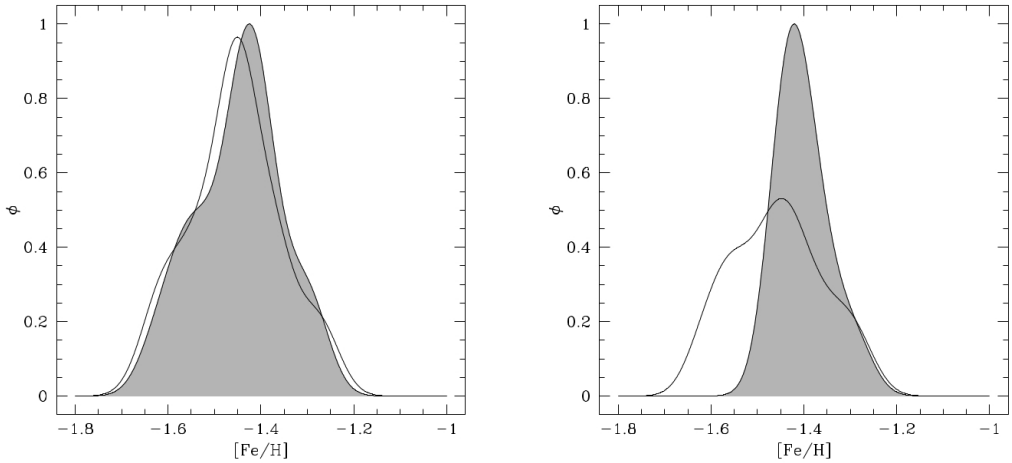

FIGURE 3.2: Left panel: Generalized histogram for [Fe I/H] (empty histogram) and [Fe II/H] (grey histogram) obtained with spectroscopic gravities. Right panel: Generalized histogram for [Fe I/H] (empty histogram) and [Fe II/H] (grey histogram) obtained with photometric gravities. Credits: A. Mucciarelli et al. (2015b, Fig. 2).

3.4. A new approach to study NGC 3201

From what was presented in Chapter 2, if variability in giant stars is in fact related to the iron spread between stars from the same cluster, it could be a possible explanation for the difference in Fe I between stars in NGC 3201 from A. Mucciarelli et al. (2015b), as well as explain the results from A. Mucciarelli et al. (2015a) were they studied M22 using the same sample from Marino et al. (2009), finding no intrinsic iron spread in the cluster but observed large differences between [Fe I/H] and [Fe II/H] in most of the stars analyzed and not only in RGB stars, in particular, there were two RGB stars (#221 and #224 from Marino et al., 2009) which even if they had very similar stellar parameters (T_{eff}, $\log g$, v_{turb} and [Fe II/H]) they displayed different [Fe I/H] abundances, which does not follow what theoretical models of NLTE calculations predicts: stars with similar parameters are expected to have the same NLTE corrections. This peculiar result might indicate that there is another mechanism that affects the iron abundance between stars even if they are have similar parameters and are at the same stage of the post-main sequence.

Chapter 4

The Generalized Lomb-Scargle and Phase Dispersion Minimization Methods

4.1. The Generalized Lomb-Scargle periodogram

The Generalized Lomb-Scargle (GLS) periodogram (Zechmeister and Kürster, 2009) is a normalization of the classical Lomb-Scargle (LS) periodogram (Lomb, 1976; Scargle, 1982), which is a very useful tool in period searches and frequency analysis of time series that is still used to this day. The LS method is equivalent to fitting sine waves of the form

$$y = a\cos\omega t + b\sin\omega t, \tag{4.1}$$

and since it provides an analytic solution for each sampled frequency this method is both efficient and convenient to use in period analysis, unlike standard fitting procedures that require the solution of a set of linear equations for each of those sampled frequencies.

When comparing the GLS to the classic LS method, the later has two inconveniences:

1. It does not take the measurement errors into account.
2. For the analysis the mean of the data is subtracted. This means that when using this method one assumes that the mean of the data and the mean of the fitted sine function are the same. The GLS solves this by adding an offset c to Eq. 4.1.

An advantage that the GLS has is that the computational effort for this method is similar as for the LS periodogram. An important characteristic

of this method is that it can be normalized. The normalization is necessary in order to determine the False Alarm Probability (FAP) of a signal which will be presented in the next section.

4.1.1. False Alarm Probability

When one is searching for a period of a given sample, one is looking at a range of frequencies with a periodogram. As such, it is important to know which periods are significant and which ones are dubious when comparing the significance of one peak compared to other peaks at different frequencies instead of the significance of a single frequency. The False Alarm Probability (FAP) is defined as

$$\text{FAP} = 1 - [1 - \text{Prob}(P > P_n)]^M \tag{4.2}$$

with P_n the power threshold for a power P and M the number of independent frequencies, this value may be estimated as the number of peaks in the periodogram. For low FAP values (FAP $<<$ 1) one can approximate Eq. 4.2 to

$$\text{FAP} = M \cdot \text{Prob}(P > P_n) \tag{4.3}$$

To determine M it is necessary to know $\delta f \approx \frac{1}{T}$ (the frequency resolution) and $\Delta f = f_2 - f_1$ the frequency range, with $M = \delta f / \Delta f$ or $M = T\Delta f$.

4.2. The Phase Dispersion Minimization method

The Phase Dispersion Minimization (PDM) (Stellingwerf, 1978) is, mathematically speaking, a type of least-squares fitting technique that consists of minimizing the dispersion of a data at a constant phase and it is also a generalization of the period determination technique by Lafler and Kinman (1965), allowing an arbitrary degree of smoothing, and providing complete statistical information.

The difference that this method has over other least-squares fitting techniques, like a Fourier component, is that instead of performing a fit on a given curve, the fit done by the PDM method is relative to the mean curve as defined by the means of each bin, and one can obtain simultaneously the best least-squares light curve and the best period. This means that that the PDM method is a kind of "Fouriergram" of infinite order, because all harmonics are included in the fitted function.

Here the basic definitions and characteristics of this method will be presented in a similar way as in Stellingwerf (1978).

4.2.1. Definitions and characteristics of the PDM method.

First we have a discrete set of observations (time-series) which can be represented by two vectors, the data (in this case magnitudes) and the observation times, denoted as x and t respectively, and there are N number of observations with the ith observation represented as (x_i, t_i). The variance of x, σ^2 is given by

$$\sigma^2 = \frac{\sum(x_i - \bar{x})^2}{N-1} \tag{4.4}$$

with $\bar{x}$ being the mean of the data x defined as $\sum x_i/N$. The sample variance s^2 for any subset of x_i is defined the same as Eq. 4.4. Then suppose that we have chosen M distinct samples, having variances s_j^2 $(j = 1, M)$ and containing n_j data points. Then as a consequence of Eq. 4.4, the overall variance for all the samples will be given by

$$s^2 = \frac{\sum(n_j - 1)s_j^2}{\sum n_j - M} \tag{4.5}$$

Since the objective is to minimize the variance of the data with respect of the mean of the light curve, we let Π be a trial period and compute a phase vector Φ: $\phi_i = t_i/\Pi - [t_i/]$ where the brackets indicate the integer part. Then, M samples from x are picked using the criteria that all the member of the sample j have the same ϕ_i. One usually divides the full phase interval (0,1) into fixed bins, but the M samples may be chosen in any way that satisfies the criteria. It is not necessary to pick all points, or a point can even belong to multiple samples. The variance of these samples gives a measure of the scatter around the mean light curve defined by the means of the x_i in each sample, considered as a function of ϕ. Finally we define the statistic quantity Θ as

$$\Theta = \frac{s^2}{\sigma^2} \tag{4.6}$$

with s^2 and σ^2 being the same the ones defined in Eq. 4.5 and Eq. 4.4, respectively. The value of Θ depends on whether Π is a true period or not. If it is not, then

$$s^2 \approx \sigma^2 \Rightarrow \Theta \approx 1,$$

but if it is then Θ will reach a local minimum compared with neighbouring periods, the closer to zero the better since the objective is, as stated previously, to minimize the dispersion of the data at a constant phase.

4.3. The *PyAstronomy* package colletion

Through the investigation, the software that was employed in order to analyze the possible variability of the light curves is the *Python*[1] software with the *PyAstronomy*[2] package collection.

4.3.1. The GLS *class*

PyAstronomy provides the user from its collection of libraries, the use of the Generalized Lomb-Scargle periodogram (Section 4.1) with the GLS *class*. It provides an implementation of the GLS periodogram introduced by Zechmeister and Kürster (2009), computing the error-weighted Lomb-Scargle periodogram using various possible normalizations. This periodogram can be controlled by the user by employing a number of keyword arguments, which will be explained within this section.

API documentation of the GLS class

This section will present the parameters of the GLS class and their properties as given in the *PyAstronomy* documentation.

```
1 PyAstronomy.pyTiming.pyPeriod.Gls(lc, fbeg=None, fend=None, Pbeg
    =None, Pend=None, ofac=10, hifac=1, freq=None, norm='ZK', ls
    =False, fast=False, verbose=False, **kwargs)
```

- **lc:** Corresponds to the *TimeSeries* instance. It can be a list, tuple or any object that provides the attribute's *time*, *flux* and (optionally) *error*. An example could be a text archive with three columns, the first one being the Date, the second the Magnitudes and the third the Errors. The argument must be a tuple, list or TimeSeries object
- **fbeg & fend:** Corresponds to the beginning and end frequencies, respectively in which the periodogram will evaluate the data, it is an optional parameter. The argument must be a *float* and the units are the inverse of the time axis of the data.
- **Pbeg & Pend:** Corresponds to the beginning and end periods, respectively in which the periodogram will evaluate the data, it is an optional parameter. The argument must be a *float* and the units are the same as the time axis of the data.
- **ofac:** Corresponds to the *Oversampling Factor*. The argument must be an *int* and the default value is $ofac = 10$.

[1] Python Software Foundation. Python Language Reference, version 2.7. Available at http://www.python.org

[2] https://github.com/sczesla/PyAstronomy

- **hifac:** Maximum frequency $freq = hifac^*$ (average Nyquist frequency). The argument must be a *float* and the default value is $hifac = 1$
- **freq:** It corresponds to a list or array that contains all the frequencies in the program will calculate the periodogram. If it is used, the parameters *fast* and *verbose* will not be available. The argument must be an *array*. The frequency array that the code generates automatically is done by employing the following equation for the frequency step

  $$f_{\text{step}} = 1.0/(\text{Time Length})/ofac$$

  with Time Length being $HJD_{\text{end}} - HJD_{\text{begin}}$ and $ofac$ the Oversampling Factor.
- **norm:** Corresponds to the normalization method that the program will employ. The options are *"ZK"* (as in Zechmeister and Kürster, 2009), *"Scargle"*, *"HorneBaliunas"*, *"Cumming"*, "wrms" (weighted root-mean square) and *"chisq"* (χ^2). The argument is a *string* and the default value is unity ("ZK").
- **ls:** This parameter allows the program to compute the classic Lomb-Scargle periodogram. The argument is a *boolean* which can be *True* or *False*, with the later being the default value.
- **fast:** This parameter allows the use of recursive relations for trigonometric functions that leads to faster evaluation. The argument is a *boolean* which can be *True* or *False*, with the later being the default value.
- **verbose:** This parameter, when used it provides some statistical outputs. The argument is a *boolean* which can be *True* or *False*, with the later being the default value.

The ***kwargs* just denotes that they are *keyword arguments*.

4.3.2. The *PyPDM class*

Apart from the *GLS* class that *PyAstronomy* provides, it also have the *Scanner* and *PyPDM* classes which are used to carry out the PDM (Section 4.2) analysis.

The ***Scanner*** class is used to establish the parameters that will be used for the PDM analysis, this means that one can define the period/frequency range and the steps used in the analysis. It is iteratable.

Meanwhile, the ***PyPDM*** class allows the user to carry out the Phase Dispersion Minimization method for period analysis presented in Section 4.2. It has various properties and methods to carry out the PDM

analysis, such as defining the number of bins that will be used, the minimum number of data points to be contained in each bin, using equidistant bins or multiple sequences of equidistant bins, which can be iterated by the user.

Parameters of *Scanner* and *PyPDM*

For the *Scanner* class

```
PyAstronomy.pyTiming.pyPDM.Scanner(minVal=0.1, maxVal=10.0, dVal
    =0.05, mode='period')
```

Its parameters are:

- **minVal & maxVal:** It denotes the minimum and maximum values of the frequency (or period) range. It is a *float* argument.
- **dVal**: Corresponds to the *delta value* of frequency (or period), in other words the step. It is a *float* argument.
- **mode:** It is an optional parameter that denotes the mode in which will carry out the PDM analysis, it can be either "period" or "frequency". The argument is a *string*, the default value is "period".

For the *PyPDM* class

```
PyAstronomy.pyTiming.pyPDM.PyPDM(time, mag)
```

Its parameters are:

- **time:** Corresponds to the time array in arbitrary units, depending on the contents of the array.
- **mag:** It is the corresponding flux (in units of magnitude) array.

Chapter 5

Relation of [Fe/H] & variability in giant stars of NGC 3201?

Authors: Á. Llancaqueo Albornoz, S. Villanova, C.C. Cortés
Collaborators: J. Ahumada, Celeste Parisi
Status: Submitted to MNRAS
Date of Submission: 25 November 2019

5.1. Abstract

We present analysis of 34 light curves, 17 in V and 17 in I filters, of 17 giant stars of NGC 3201 which were previously studied for their iron abundance, with the objective to check if there is a relation between variability and iron abundance of the stars. We computed the GLS and PDM periodograms on the sample in order to check if the stars were variables. From the sample, 8 stars were discarded from being variable, 3 were considered as possible candidate variables and 6 stars displayed variable behaviour with periods ranging from 0.0881 ± 0.0001 to 0.5418 ± 0.0027 days. These variable stars showed distinct values of [Fe I/H], the 3 most metal-rich stars being RGB, one star with [Fe I/H] $= -1.37$ and two with [Fe I/H] $= -1.31$ dex. The two most metal-poor variables have [Fe I/H] $= -1.61$ and [Fe I/H] $= -1.62$ dex and are AGB stars and one variable showed [Fe I/H] $= -1.50$ dex also being an AGB star. Meanwhile stars that were non-variables showed $-1.56 \leq$ [Fe I/H] ≤ -1.40. We conclude that variability affects somehow the spectroscopic determination of the iron content of giant stars in globular clusters.

5.2. General Information of the data

The data utilized in this investigation are 34 light curves which were provided by Javier Ahumada and his team from the work done in Arellano Ferro et al. (2014), with 17 being for the V filter (Figure 5.1) and 17 for the I filter (Figure 5.2) from the Johnson-Cousin photometric system, with each pair of light curves being associated to a star. A sample of the contents of the light curves are shown in Table 5.1, labeled in the same way as in Arellano Ferro et al. (2014).

TABLE 5.1: Sample time series for V and I filters of each star. Column (1) and (2) display the ID of the star and the filter, respectively. Column (3) shows the epoch of mid-exposure in heliocentric Julian days (HJD), columns (4) and (5) shows the standard $M_{\rm std}$ and instrumental magnitudes $m_{\rm ins}$, respectively. Column (6) is the errors associated to both the instrumental and standard magnitudes. Columns (7), (9) and (11) displays the reference and differential fluxes $f_{\rm ref}$ and $f_{\rm diff}$ and the scale factor p, respectively and columns (8) and (10) show the uncertainties $\sigma_{\rm ref}$ and $\sigma_{\rm diff}$.

Star	Filter	HJD (d)	$M_{\rm std}$ (mag)	$m_{\rm ins}$ (mag)	σ_M (mag)	$f_{\rm ref}$ ADU s^{-1}	$\sigma_{\rm ref}$ ADU s^{-1}	$f_{\rm diff}$ ADU s^{-1}	$\sigma_{\rm diff}$ ADU s^{-1}	p
N° 1	V	2456371.522859	13.93920	15.14176	0.00074	08893.86188	8.22988	−117.46357	05.97238	+0.99657
N° 1	V	2456371.525984	13.94512	15.14768	0.00063	08893.86188	8.22988	−165.73297	05.07454	+1.00063
⋮	⋮	⋮	⋮	⋮	⋮	⋮	⋮	⋮	⋮	⋮
N° 1	I	2456371.517222	12.62022	14.38817	0.00085	17683.53084	7.28054	−096.54252	13.87334	+1.00304
N° 1	I	2456371.519717	12.61734	14.38529	0.00080	17683.53084	7.28054	−049.80669	13.03557	+1.00472
⋮	⋮	⋮	⋮	⋮	⋮	⋮	⋮	⋮	⋮	⋮
N° 2	V	2456371.522859	12.89581	14.08926	0.00043	22955.43000	8.35538	+180.37899	09.05216	+0.99657
N° 2	V	2456371.525984	12.89554	14.08899	0.00035	22955.43000	8.35538	+186.76700	07.45875	+1.00063
⋮	⋮	⋮	⋮	⋮	⋮	⋮	⋮	⋮	⋮	⋮
N° 2	I	2456371.517222	11.36980	13.13381	0.00043	55690.04870	7.18612	+150.05747	22.14350	+1.00304
N° 2	I	2456371.519717	11.37122	13.13523	0.00041	55690.04870	7.18612	+076.86635	21.18071	+1.00472

Figure 5.3 displays the finding chart where all 17 giant stars from NGC 3201 are, marked with cyan open circles.

5.3. Observations and Data Management

5.3.1. Observation and data origin

The Johnson-Kron-Cousins V and I photometric observations were obtained on March 20-23, 2013 by the team of Javier Ahumada and Arellano Ferro, at the Complejo Astronómico El Leoncito (CASLEO), San Juan, Argentina, using the 2.15-m telescope and the detector used was a Roper Scientific back-illuminated CCD of 2048 × 2048 pixels with a scale of 0.15 arcsec/pix and a Field of View of approximately 5.1 × 5.1 arcmin^2.

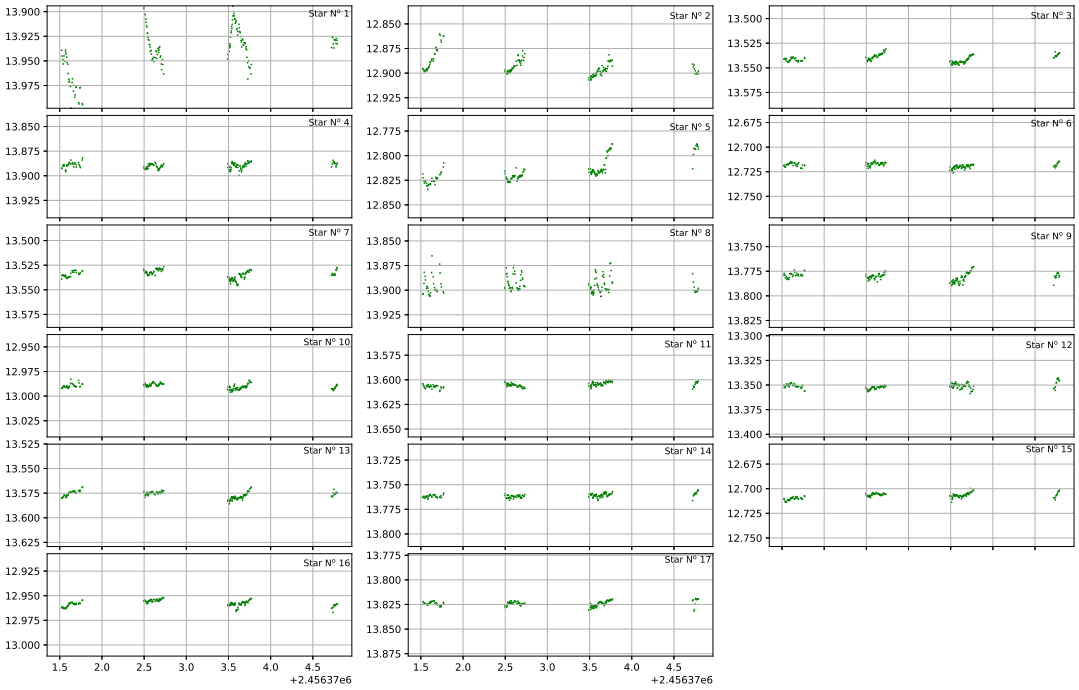

FIGURE 5.1: Light curves of each star for V filter plotted with the same scale as Star N° 1 (top left panel), all light curves are labeled as 'Star N°...´ from 1 to 17 starting with the top left panel following from left to right. The x-axis of each plot correspond to the Heliocentric Julian Days (HJD) and the y-axis is the standard magnitude V.

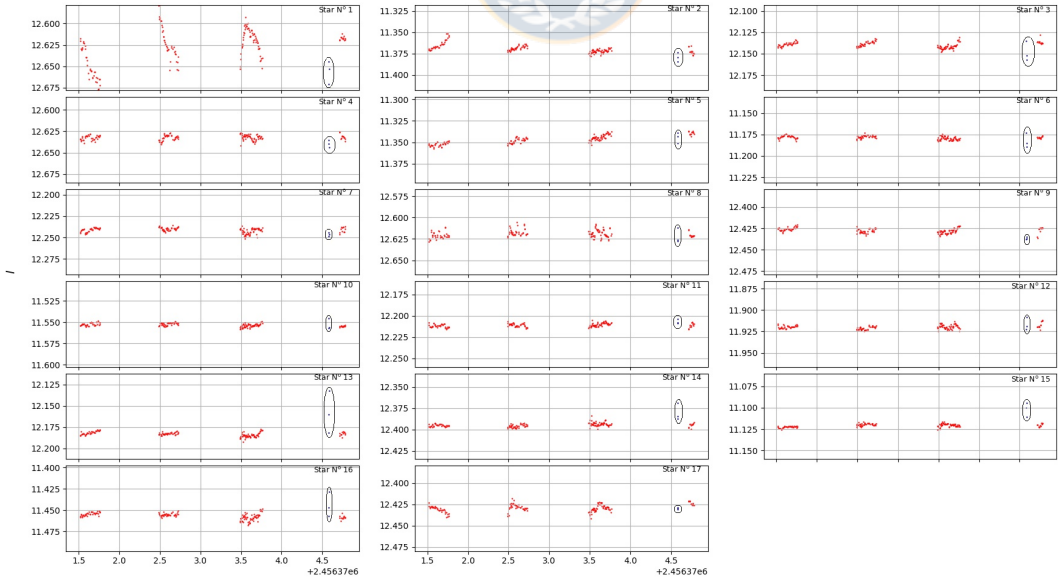

FIGURE 5.2: Light curves of each star for I filter plotted with the same scale as Star N° 1 (top left panel), all light curves are labeled as 'Star N°...´ from 1 to 17 starting with the top left panel following from left to right. The x-axis of each plot correspond to the Heliocentric Julian Days (HJD) and the y-axis is the standard magnitude I. The three blue points are observations taken on the fourth night that were not considered for the analysis, which will be explained later.

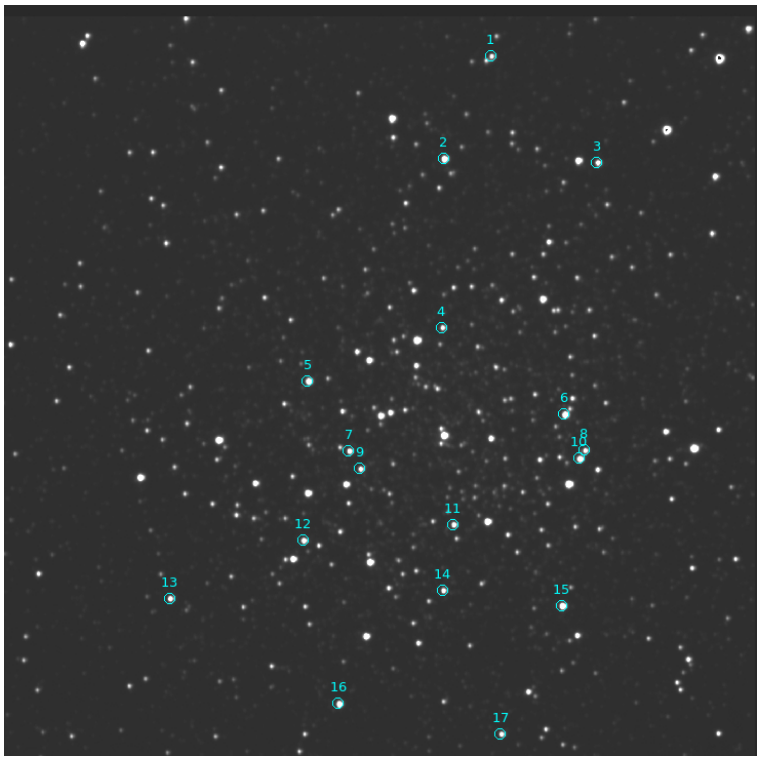

FIGURE 5.3: Finding chart of the 17 giant stars analyzed in this work, with each one marked with cyan open circles. The number next to each star are the numbers used for their ID.

5.3.2. Data Processing

Image data was calibrated using bias and flat-field correction procedures, which were done previously by Arellano Ferro, Javier Ahumada and their team (Arellano Ferro et al., 2014). They used Difference Image Analysis (DIA) to extract high-precision time-series photometry in the field of NGC 3201, were they used the DanDIA[1] pipeline for the data reduction process (Bramich et al., 2013), which includes an algorithm that models the convolution kernel matching the PSF of a pair of images of the same field as a discrete pixel array (Bramich, 2008).

In Arellano Ferro et al. (2014), the authors also employed the methodology developed by Bramich and Freudling (2012) to solve for the magnitude offset. Such offset can reach up to $\approx$ 30 mmag in a few cases, but it is generally of the order of $\approx 1 - 10$ mmag. The correction made helped them to improve the quality of the light curves, particularly for the brightest stars of the cluster.

To transform the instrumental magnitudes into the standard Johnson-Kron-Cousins photometric system (Landolt, 1973), the authors identified 85 standard stars of Stetson (2000)[2] in the Field of View (FoV) of their

[1] DanDIA is built from the DanIDL library of IDL routines available at http://www.danidl.co.uk
[2] http://www3.cadc-ccda.hia-iha.nrc-cnrc.gc.ca/community/STETSON/standards

images with V and V-I in the ranges 12.6-18.6 mag and -0.14-1.01 mag, respectively. The transformation equations are of the form:

$$V = v + 0.0440(\pm 0.0076)(v-i) - 1.2353(\pm 0.0054), \quad (5.1)$$

$$I = i + 0.0190(\pm 0.0089)(v-i) - 1.7821(\pm 0.0064). \quad (5.2)$$

5.3.3. Identifying each star

The next step was match each star with the ones from A. Mucciarelli et al. (2015b) in order to identify them. To do this, we matched the position (RA and DEC) of each star and calculated the mean magnitudes $\langle M_V \rangle$ and $\langle M_I \rangle$ for V and I filters, respectively. Table 5.2 shows the main information of the each stars, that information being position, mean magnitude for each filter and their Fe I and Fe II abundances from A. Mucciarelli et al. (2015b). Figure 5.4 shows the CMD of the cluster with all stars studied in this work labeled with different markers depending on how they were classified, which will be explained in Section 5.4.2 and Section 5.5. A thing to note is that there were no attempt to deredden the CMD due to the differential nature of the reddening in front of the cluster.

TABLE 5.2: Main information of the 17 giant stars studied in this work. Col. 1 shows the number of their corresponding light curve from Fig. 5.1 and Fig. 5.2 of this work, col. 2 and col. 7 shows the ID of each star and their [Fe/H] values from Simmerer et al. (2013) and col. 8 and col. 9 are the [Fe I/H] and [Fe II/H] values from A. Mucciarelli et al. (2015b) obtained by employing photometric gravities. Col. 5 and col. 6 are the mean magnitudes for V ($\langle M_V \rangle$) and I ($\langle M_I \rangle$) filters, measured from the data of the light curves of each star. The stars that are marked with $*$ are the one which we determined as variable stars.

Star N°	ID	RA (J2000)	DEC (J2000)	$\langle M_V \rangle$ (mag)	$\langle M_I \rangle$ (mag)	[Fe/H] (dex)	[Fe I/H] (dex)	[Fe II/H] (dex)
1*	105	154.3433125	−46.4197750	13.94	12.63	−1.48	-1.31 ± 0.03	-1.29 ± 0.05
2*	124	154.3596208	−46.4137333	12.89	11.37	−1.42	-1.37 ± 0.02	-1.40 ± 0.05
3	129	154.3617667	−46.4310361	13.54	12.14	−1.54	-1.48 ± 0.02	-1.43 ± 0.04
4*	181	154.3872500	−46.4123778	13.89	12.63	−1.79	-1.62 ± 0.03	-1.37 ± 0.04
5*	200	154.3946708	−46.3968944	12.82	11.35	−1.53	-1.50 ± 0.02	-1.40 ± 0.04
6	222	154.4027208	−46.4256111	12.72	11.18	−1.45	-1.47 ± 0.02	-1.45 ± 0.05
7	231	154.4065292	−46.4010306	13.53	12.24	−1.65	-1.54 ± 0.02	-1.39 ± 0.03
8*	240	154.4087875	−46.4276361	13.89	12.62	−1.71	-1.61 ± 0.03	-1.38 ± 0.04
9	244	154.4095667	−46.4021667	13.78	12.43	−1.56	-1.44 ± 0.02	-1.44 ± 0.05
10	249	154.4101042	−46.4269639	12.99	11.55	−1.64	-1.56 ± 0.02	-1.42 ± 0.04
11	277	154.4196083	−46.4122944	13.61	12.21	−1.50	-1.40 ± 0.02	-1.42 ± 0.05
12	279	154.4207125	−46.3952389	13.35	11.92	−1.54	-1.43 ± 0.03	-1.43 ± 0.04
13	303	154.4288708	−46.3798167	13.58	12.18	−1.51	-1.45 ± 0.02	-1.45 ± 0.04
14	308	154.4302625	−46.4106583	13.76	12.39	−1.52	-1.50 ± 0.02	-1.45 ± 0.04
15	312	154.4340000	−46.4239750	12.71	11.12	−1.46	-1.44 ± 0.03	-1.44 ± 0.06
16	332	154.4478125	−46.3981083	12.96	11.46	−1.59	-1.54 ± 0.02	-1.38 ± 0.04
17*	344	154.4543542	−46.4162194	13.82	12.43	−1.45	-1.31 ± 0.03	-1.29 ± 0.05

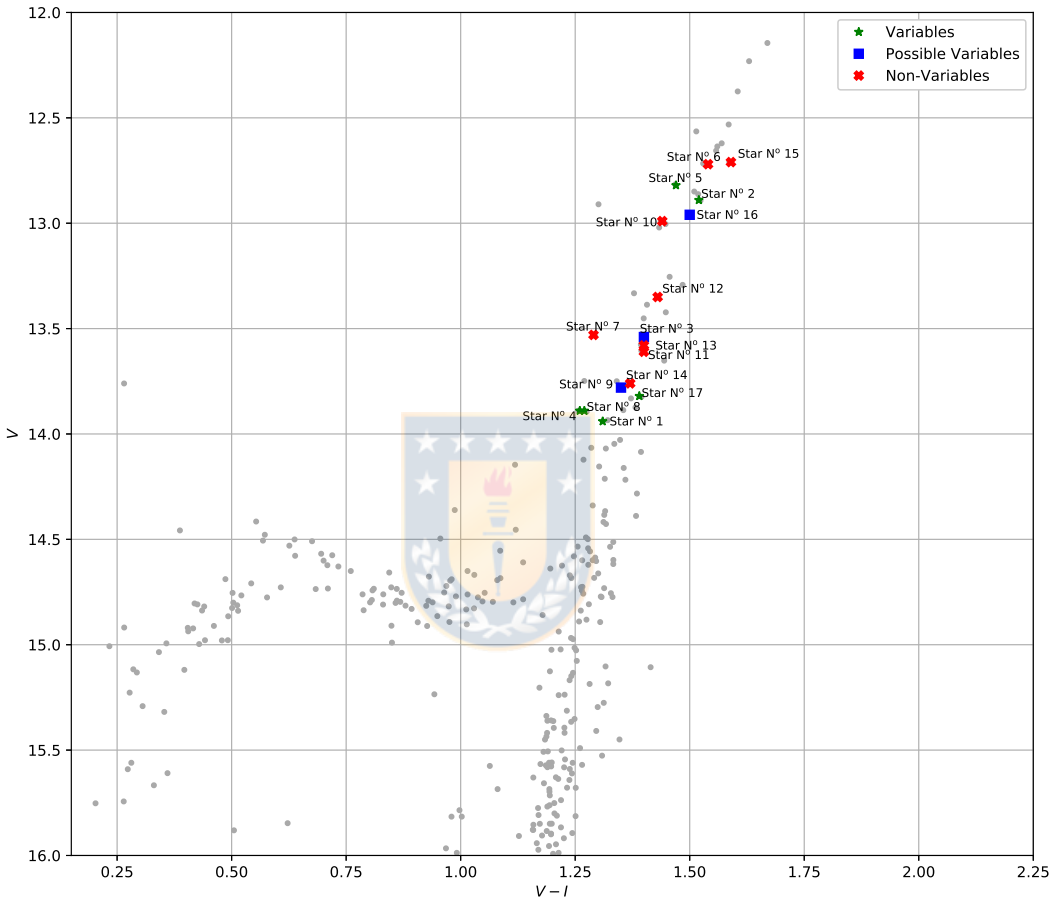

FIGURE 5.4: CMD of NGC 3201 displaying the 17 stars studied in this work with different markers based on their classification. Green stars are the variable stars, blue squares the possible variables and the red crosses are the non-variables. Each star also have their corresponding ID next to it.

5.4. Analysis of the Light Curves

The methodology employed to check and analyze the possible variable behaviour of each star from their light curve data was the application of both the Generalized Lomb-Scargle periodogram (Zechmeister and Kürster, 2009) and the Phase Dispersion Minimization method (Stellingwerf, 1978). The computing of each method was done by using the *PyAstronomy* package from *Python* (Section 4.3). Appendix A presents the full code that was used to compute both the GLS and PDM methods, along with an explanation of each step in order to clarify what the code did and Figure A.2 shows the resulting periodograms of each method for V and I filters. An important thing to note is that for all stars in the I filter there are 3 epochs taken in the fourth night which are indicated with a circle in Figure 5.2. These epoch show evidence to have been affected by bad photometry and were rejected as outliers.

5.4.1. Preliminary discarding process

In order to check which giant star could be a candidate variable star and which ones should be discarded, the following criteria was adopted:

- The amplitude $A \pm \sigma_A > \text{rms}_M$ for both filters. With σ_A and rms_M being the amplitude error and the weighted root-mean square of the dataset (this is the average error), respectively. The reason for this is that: If the rms_M is equal or even higher than the amplitude A it would mean that the supposed variability of the star is just the errors of the magnitude measurement. These parameters are obtained from the GLS analysis (see Figure A.1).
- The possible periods display their peaks above the False Alarm Probability (FAP) threshold of 0.1% in the GLS periodogram for both filters.
- $P_{\text{GLS}} \sim P_{\text{PDM}}$ for both filters.
- The possible period is present in both V and I filters ($P_V \sim P_I$).
- Visual analysis, which means to look each light curve and check which stars for both V and I filters displayed a constant magnitude during the four nights of observation.

From this preliminary analysis and discarding criteria, stars N° 6, N° 7, N° 10, N° 12, N° 14 and N° 15 were classified as non-variable and as such were discarded.

5.4.2. The Significance Test

After finishing the previous analysis and discarding process for all 17 stars, the next step was to calculate the magnitude difference ΔM for each star given by

$$\Delta M = M - \langle M \rangle \tag{5.3}$$

with M being the magnitude of the star in each epoch and $\langle M \rangle$ the mean magnitude of the star from the complete data of its light curve. As in the preliminary analysis, the 3 bad data points of the fourth night in the I filter (indicated with a circle around them in Figure 5.2) affected the measurement of $< M_I >$ and, in consequence, ΔM_I, due to that we decided to discard those 3 points from the analysis.

After calculating ΔM for all 17 giant stars, we calculated

$$\sigma_M{}^{3} = \sqrt{\frac{\sum \Delta M^2}{N-1}}$$

and its error

$$err_\sigma = \frac{\sigma}{\sqrt{N}}$$

for all six targets that were discarded as non-variables using the data of all those stars combined for each filter separately, which we named $\sigma_{\text{Non Var.}}$ and $err_{\sigma_{\text{Non Var.}}}$ respectively. Then, we calculated σ_{Star} and $err_{\sigma_{\text{Star}}}$ for the rest of the eleven candidate variable stars individually, in order to determine their Significance S (for each filter), given by

$$S = \frac{\sigma_{\text{Star}} - \sigma_{\text{Non Var.}}}{\sqrt{err^2_{\sigma_{\text{Star}}} + err^2_{\sigma_{\text{Non Var.}}}}} \tag{5.4}$$

To determine whether or not the star could be classified as a variable the following criteria was adopted depending of the value of S that each star obtained from Eq. 5.4:

1. If $S < 2$ for both filters, the star is classified as non-variable.
2. If $S > 3$ for both filters, the star is classified as variable.
3. If $S > 3$ in one of the filters, the star is classified as possible variable.
4. If $2 < S < 3$ in one or both filter, the star is classified as a dubious variable and requires further re-analysis.

Depending on which case each star were found, a re-analysis of their light curves could be performed or not. All stars that were found in the case (1) of the significance test were discarded from the re-analysis since

[3] Note: this quantity σ_M is different from the one presented in Table 5.1

they were classified as non-variables. For the stars that were found in the cases (2), (3) and (4), they were re-analyzed by performing the period analysis previously detailed in Section 4. The most important cases for the re-analysis were those stars that were found in cases (3) and (4), because depending on the re-analysis they could be either confirmed to be a variable star, considered as a possible study object for future time-series analysis.

Table 5.3 shows the significance obtained for all eleven candidate variables along with the classification given by the criteria explained previously. From the results that are presented in this Table: 2 stars were discarded from being variable stars (N° 11 and N° 13) due to their low values of S_V and S_I, being both lower than 2. 4 star were classified as Variables (N° 1, N° 2, N° 5 and N° 8) since $S_V > 3$ and $S_I > 3$ for each star and their light curves from Figure. 5.1 and Figure. 5.2 shows a clear change in their magnitudes during each night of observation. 4 stars were classified as **Possible Variables** (N° 3, N° 9, N° 16 and N° 17) and were re-analyzed to see if they could be a variable or maybe a candidate for future investigations. Finally, only one star was catalogued as **Dubious**, Star N° 4, for which was required a deeper and focused re-analysis in order to either discard it from being a variable star or be considered as a variable or even possible candidate.

TABLE 5.3: Significance S values for V and I filter for all eleven candidate variable stars along with their classification regarding the adopted criteria from the Significance Test

Star	S_V	S_I	Classification
N° 1	10.435	10.526	Variable
N° 2	8.288	5.834	Variable
N° 3	2.467	3.503	Possible
N° 4	0.346	2.720	Dubious Variable
N° 5	8.919	6.151	Variable
N° 8	7.863	5.521	Variable
N° 9	3.386	2.253	Possible
N° 11	~ 0	~ 0	Non-Variable
N° 13	1.749	0.712	Non-Variable
N° 16	0.631	4.058	Possible
N° 17	~ 0	5.336	Possible

5.5. Results

In this section the results for all 9 stars that were considered for re-analysis from the results presented in Table 5.3 from Section 5.4.2 are presented, were we distinguished those who are candidate variables and possible candidates based on the re-analysis of each star individually.

5.5.1. Variable Stars

This section presents all stars that were confirmed as variable from both the results of the significance test and the re-analysis of their light curves. Table 5.4 shows the main parameters of all stars that were classified as variables from our period analysis and Figure 5.5[4] shows the phased light curves of all variables stars that were found in this work. To phase each light curve, the following expression was used:

$$\phi = \left(\frac{T}{P} - T_0\right) - \left[\frac{T}{P} - T_0\right] \tag{5.5}$$

with T being the observation time, P period of the star and T_0 the zero point. The brackets in the second of the right side of Eq. 5.5 indicate the integer part. Appendix B shows the *Python* code used to make these plots.

TABLE 5.4: Parameters for all stars that presented a variable behaviour. The first column displays the ID of the star. Second and sixth columns shows the periods P_V and P_I obtained from the analysis in both V and I filters respectively in units of days, along with their respective error σ_{P_V} and σ_{P_I} on the third and seventh column. The fourth and eighth column displays the amplitude A for V and I filters, and their errors $\sigma_{A(V)}$ and $\sigma_{A(I)}$ are shown in the fifth and ninth column. The mean magnitudes $\langle M_V \rangle$ and $\langle M_I \rangle$ for V and I filters are displayed in the tenth and eleventh column.

Star	P_V (days)	σ_{P_V} (days)	$A(V)$ (mag)	$\sigma_{A(V)}$ (mag)	P_I (days)	σ_{P_I} (days)	$A(I)$ (mag)	$\sigma_{A(I)}$ (mag)	$\langle M_V \rangle$ (mag)	$\langle M_I \rangle$ (mag)
N° 8	0.0881	0.0001	0.0195	0.0012	0.0881	0.0002	0.0072	0.0004	13.8944	12.6193
N° 1	0.5418	0.0027	0.0591	0.0025	0.5417	0.0023	0.0556	0.0021	13.9393	12.6293
N° 2	0.5329	0.0026	0.0266	0.0012	0.5417	0.0043	0.0116	0.0008	12.8925	11.3689
N° 5	0.4827	0.0024	0.0331	0.0013	0.4772	0.0034	0.0114	0.0009	12.8158	11.3473
N° 17	0.3535	0.0035	0.0045	0.0005	0.3535	0.0021	0.0093	0.0007	13.8238	12.4290
N° 4	0.1628	0.0008	0.0047	0.0005	0.1628	0.0007	0.0053	0.0006	13.8897	12.6326

Star N° 8

This star displays a period of $P = 0.0881 \pm 0.0001$ days in both filters, it was the one that presented the most distinguished magnitude difference

[4]The period used to phase all light curves was the one obtained from the analysis in V filter, P_V.

from its light curves as seen from Figure 5.1 and Figure 5.2, along with Star N° 1. The results from the period analysis mentioned in Section 5.4 were straightforward and the periods obtained from each method were equal if not similar, as seen in Figure A.2b where in the I filter (right panels), the GLS periodogram marked a peak in $P_I = 0.0811$ while the PDM method marked $P_I = 0.0881$, but in the same figure we can see that the second highest peak in GLS corresponds to the period marked in the PDM method, which has the same value as P_V. The last step that was used to discriminate which period was the correct one was to phase the light curve using both periods from the I filter. Figure 5.5a shows the phased light curve of this star for V and I filters.

Furthermore, due to this consistency in the results from both methods, most of the parameter testing in the code (Appendix A) were realized with this star.

Star N° 1

This star displays a period of $P = 0.5418 \pm 0.0027$ days, with an amplitude $A > 0.055$ mag in both filters, apart from displaying a clear variable behaviour as seen in Figure 5.1 and Figure 5.2, along with a clear phased light curve displayed in Figure 5.5b. For the case of this star, at first during the analysis for V filter the GLS analysis showed us a period of 1.1136 days if we considered a $P_{end} =$ Time Length $= 3.2$, but the PDM analysis marked $P_V \sim 0.5510$, while in the I filter both the GLS and PDM analysis displayed a period between 0.5413 and 0.5546. From this discrepancy of each method, we began to restrict the value of P_{end} and re-evaluate. This was done until the maximum period would be $P \leq 1$ day, and from this restriction we obtained the parameters shown in Table 5.4.

Star N° 2

This star, like the cases of Star N° 8 and Star N° 1 displayed an evident magnitude difference, which can be seen in both of its light curves. For this case, the period analysis showed that this star have a period $P = 0.5329 \pm 0.0026$, but in the phased LC shown in Figure 5.5c it does not display a complete sinusoidal curve. This might be due to lack of coverage during the day, where the observations were not carried out.

Star N° 4

This star was the most interesting case, since it was classified as a dubious variable due to the significance values from Table 5.3. Due to this, we

re-performed our period analysis with more caution and detail. From the analysis, this star showed in both filters similar values of P from the GLS method but differing with the PDM method due to the Pbeg and Pend range, which at first had a value of $P_{end} = 1$ but after restricting their values (taking caution that both periodograms do not display the estimated period as the only possible one) both methods showed similar values of $P = 0.1628 \pm 0.0008$, and from the re-analysis and subsequent phasing of its light curve we confirmed that this star was a variable, although with a very low amplitude. The final results shown in Table 5.4 and the phased light curve of this star can be seen in Figure 5.5d.

Star N° 5

This star shows a quite clear variable behaviour in its LC from Figure 5.1, whereas in Figure 5.2 it does not present an evident variable behaviour if we compare directly between filters. The variability analysis showed that this star have a period $P = 0.4827 \pm 0.0024$ and its phased light curve is shown in Figure 5.5e.

Star N° 17

Same as with Star N° 4, this star was also a peculiar case, since it's LC for V filter did not display an evident variable behaviour, but in the I filter it showed a notorious variability in magnitude, which can be seen in its LC from Figure 5.2. Furthermore, its S_I value from Table 5.3 was higher that 3 but its $S_V < 2$, which made us to initially classify it as a possible variable. After re-performing our period analysis for this star, we obtained the period $P = 0.3535 \pm 0.0035$, amplitudes $A(V)$ and $A(I)$ shown in Table 5.4 and from its phased light curve we finally classified this star as a variable. The phased light curve of this star is shown in Figure 5.5f.

5.5.2. Possible Candidate Variable Stars

In this part, all stars that were considered as *possible* candidate variables are discussed individually. These stars were classified as such due to: their S_V and S_I values obtained from the Significance Test displayed shown in Table 5.3 and because from the re-analysis of their light curves it was not possible to determine in a valid way to be a variable star, but also they were clearly not non-variables.

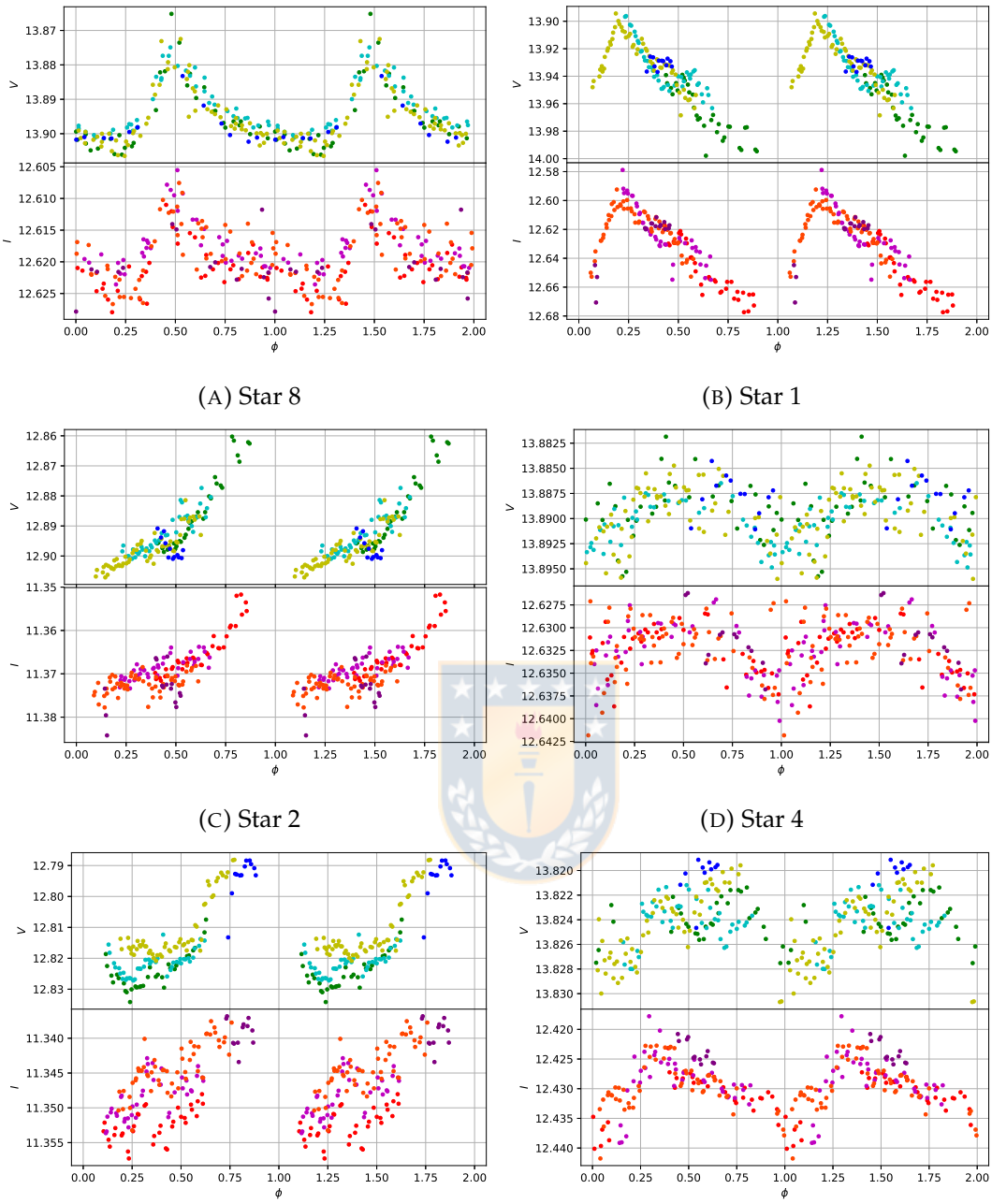

(A) Star 8

(B) Star 1

(C) Star 2

(D) Star 4

(E) Star 5

(F) Star 17

FIGURE 5.5: Phased light curves of all 6 variable stars found in this work, which were plotted by phasing the LC of each star with their corresponding period shown in Table 5.4. The top panel of each phased light curve correspond to the V filter and the bottom panel the I filter. The different colors are to denote the data taken during each night of observation, for the top panels: Night 1 is green, Night 2 cyan, Night 3 yellow and Night 4 blue. For the bottom panels: Night is 1 red, Night 2 magenta, Night 3 orange and Night 4 purple. The phase zero is defined so that the curve can be appreciated clearly and it is not the same for each curve.

Star N° 3

This star was classified as a Possible Variable due to its values of $S_V = 2.467$ and $S_I = 3.503$ from the significance test that was performed. Due to this, its light curves were re-analyzed in order to check if it could be in fact a variable star or if it should be discarded definitely. From the re-analysis between filters, for this star we found a possible period $P = 0.3528$ with Figure 5.6 displaying the phased light curve using said period. This particular period is subject to errors since its LC could lead to another solution. A possible way to determine a more precise period could be obtaining a more complete time series observations for this star.

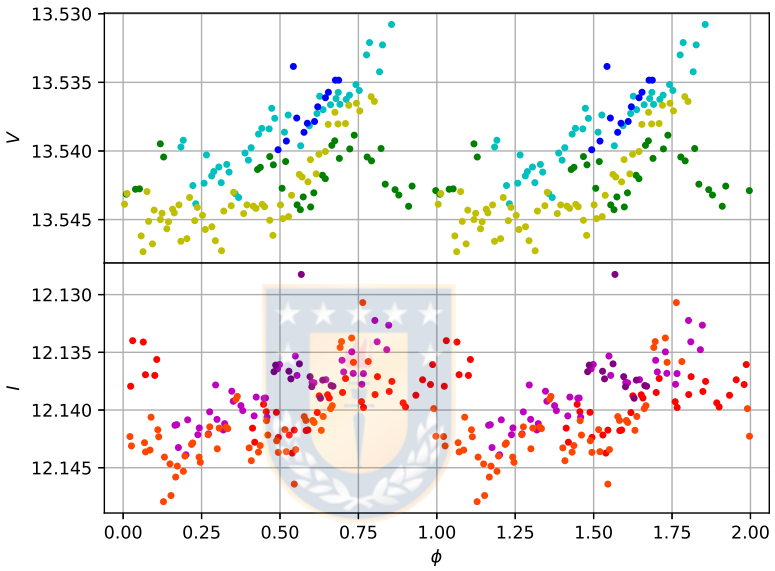

FIGURE 5.6: Top panel: Phased Light Curve of Star N° 3 for V filter, plotted by phasing the light curve with a period $P = 0.3528$ days. The different colors are the same as the one presented in Figure 5.5. Bottom panel: Phased Light Curve of Star N° 3 for I filter. Same as in previous figures, the different colors are the same ones from Figure 5.5.

Star N° 9

This star displayed in its V filter LC (3rd row and 1st column panel from Figure 5.1) a peculiar (possible) variable behaviour, but in its I filter LC (3rd row and 1st column panel from Figure 5.2) was not that evident. After performing our analysis, the most probable period for the V filter was $P = 0.5281$ days, and in the I filter, even though the GLS analysis marked a similar period as the most probable, PDM analysis marked a period of $P \sim 0.3417$ days, unless we restricted the values of Pbeg and Pend so that there was only one possible period. Figure 5.7 display the phased light curve for this possible candidate variable.

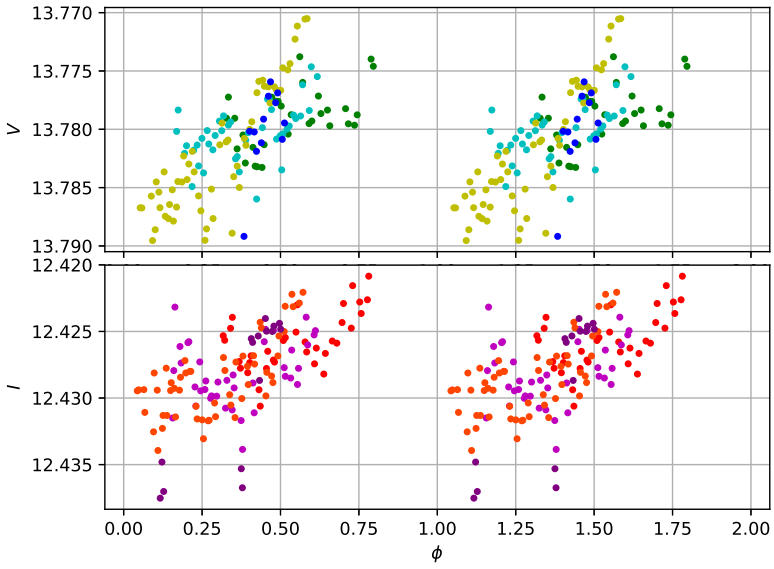

FIGURE 5.7: Top panel: Phased Light Curve of Star N° 9 for V filter, plotted by phasing the light curve with a period $P = 0.5281$ days. Again, the different colors are the same as in Figure 5.5. Bottom panel: Phased Light Curve of Star N° 9 for I filter. Same as in previous figures, the different colors are the same as in Figure 5.5.

Star N° 16

This particular star was a bit challenging since its LC for V filter did not present an evident magnitude difference between each night, but for the I filter it displayed a peculiar behaviour during the 3rd night. From our period analysis V and I displayed periods close between each filter $P_V = 0.3981$ days (left panels of Figure 5.8) and $P_I = 0.4174$ days (right panels of Figure 5.8), which we evaluated by phasing the LCs using both periods. From the results in its significance values from Table 5.3 and since it is not clear to define which period is correct between the two already mentioned, this star was regarded as a possible variable. Future observations for this star could help to determine if one of those periods is the correct one or it could be an entirely different period.

5.6. [Fe/H]-variability relation and Conclusions

From the results shown in Section 5.5, the next step was to revise the literature from NGC 3201 regarding its iron abundance, specifically Simmerer et al. (2013) and A. Mucciarelli et al. (2015b). Since each star was previously identified (Section 5.3.3) we matched all stars that were variable, non-variable and possible variables with their respective iron abundance from literature in order to check if there is a relationship between [Fe/H] and variability of the star. In A. Mucciarelli et al. (2015b), the

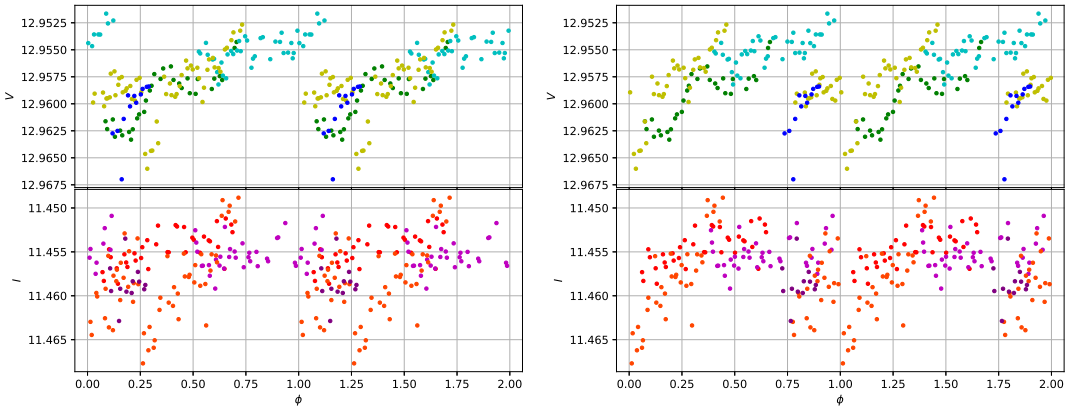

FIGURE 5.8: Left panels: Phased Light Curve of Star N° 16 for V (top panel) and I (bottom panel) filters, plotted by phasing the light curve with the period obtained from our analysis in the V filter $P_V = 0.3981$ days. Right panels: Phased Light Curve of Star N° 16 for V (top panel) and I (bottom panel) filters, plotted by phasing the light curve with the period obtained from our analysis in the in the I filter $P_I = 0.4174$ days. As in previous figures, the different colors shown in all panels are the same as in Figure 5.5.

authors measured the iron abundance of NGC 3201 by adopting both spectroscopic values of $\log g$ with the same methodology as in Simmerer et al. (2013) as well as photometric values of $\log g$ by following a similar approach as in Lapenna et al. (2014). Their reasons for using photometric gravities was due to the results from the later work from Lapenna, were the authors pointed out that NLTE effects in AGB stars affect the abundances that are obtained from Fe I lines lowering them, but the abundances from Fe II lines are not affected, and such effect can be detected by assuming photometric values of $\log g$ and measuring the abundances from Fe I and Fe II independently. Furthermore, the authors also point out that RGB stars do not display such effects, meaning that independently of using spectroscopic or photometric gravities the abundances that are obtained for RGB stars should be similar since they are not affected by such NLTE effects in comparison with AGB stars.

5.6.1. Comparing the iron abundance between variables and non-variables

From the revision that was carried out as well from the information presented in both Table 5.2 and Table 5.4, there are two main features that can be noted:

1. All 6 stars that show variable behaviour and were confirmed as variables have a common feature: They display extreme values of [Fe I/H] (if we compare their metallicity with the rest of the sample)

with only one star being the exception of this feature being Star N° 5. Furthermore, from these stars there is another feature that can be taken in consideration, and it is that all variable stars that are more metal-poor (being Star N° 4 and Star N° 8) along with Star N° 5 are AGB stars; whereas all stars that were more metal-rich (Stars N° 1, 2 and 17) are RGB stars, as seen in Figure 5.4.

2. All stars that were not variable and those which are possible candidate variables display [Fe I/H] measurements that are closer to the mean value of the total sample of stars [Fe I/H] ≈ -1.47 dex.

The left panel of Figure 5.9 presents in a graphical way the relationship between [Fe I/H] and variability of a star that was obtained from this work showing the iron abundances that A. Mucciarelli et al. (2015b) obtained by using photometric $\log g$. We also revised the [Fe II/H] content of each star to see if there could also be a relation between its abundance and the variability of the giant stars, which can be seen in the right panel of Figure 5.9. From this histogram we can see that the variable stars tend to have higher [Fe II/H] values compared with the non-variable stars.

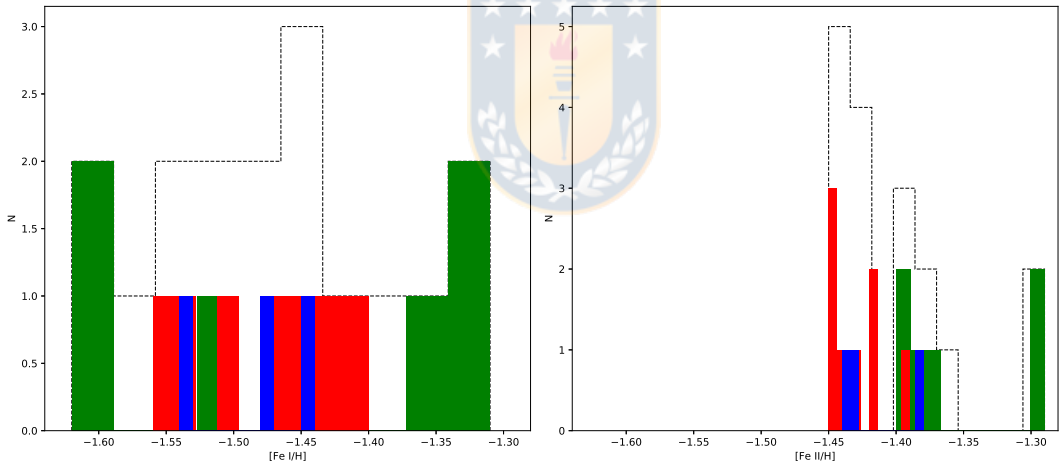

FIGURE 5.9: The distribution of both neutral iron (left panel) and ionized iron (right panel) abundances from A. Mucciarelli et al. (2015b) showing the relationship between stars classified as variables (green histogram), possible variables (blue) and non-variables (red) with their iron abundance.

For further confirmation of this relation we revised the Fe abundances of the same stars that were obtained from the spectroscopic analysis of Simmerer et al. (2013) to check if their abundances derived from spectroscopic $\log g$ and their assumption of ionization balance between Fe I and Fe II lines display a different kind of relationship between iron abundance and variability. Figure 5.10 shows the distribution of [Fe/H] from Simmerer et al. (2013) along with the relationship between variability and the abundance.

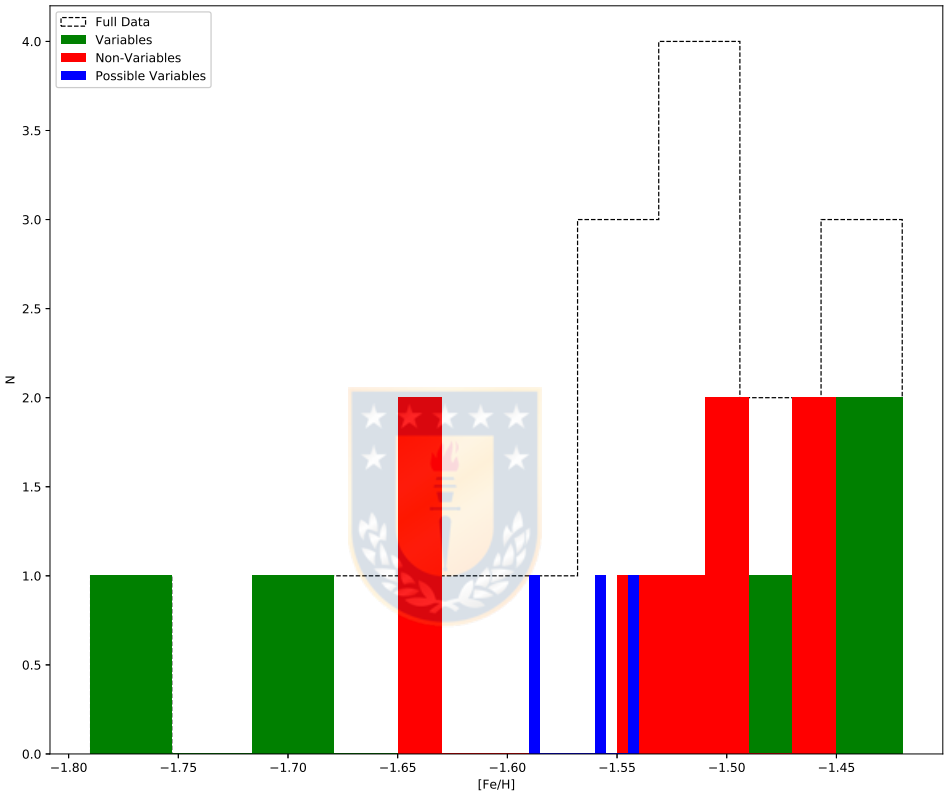

FIGURE 5.10: The distribution of [Fe/H] with the abundances from Simmerer et al., 2013. As in Figure 5.9, stars that display variable behaviour (in general) are the ones that display extreme values of [Fe/H], whereas those that are non-variable and possible variables display abundances closer to the mean of the total sample. The black dashed lines in both panels shows the distribution of the complete sample.

Table 5.5 summarizes what was presented by showing the classification of all 17 stars along with the different iron abundance measurements of each from Simmerer et al. (2013) and A. Mucciarelli et al. (2015b).

TABLE 5.5: Iron abundance information of the 17 giant stars. Col. 1 shows the ID of the star, col. 2 displays the final classification of the star (Variable, Possible or Non-Variable). Col. 3 and col. 4 displays the [Fe I/H] and [Fe II/H] values from A. Mucciarelli et al. (2015b), respectively and col. 5 shows the [Fe/H] values from Simmerer et al. (2013).

Star	Classification	[Fe I/H] (dex)	[Fe II/H] (dex)	[Fe/H] (dex)
1	Variable	-1.48	-1.31 ± 0.03	-1.29 ± 0.05
2	Variable	-1.42	-1.37 ± 0.02	-1.40 ± 0.05
3	Possible	-1.54	-1.48 ± 0.02	-1.43 ± 0.04
4	Variable	-1.79	-1.62 ± 0.03	-1.37 ± 0.04
5	Variable	-1.53	-1.50 ± 0.02	-1.40 ± 0.04
6	Possible	-1.45	-1.47 ± 0.02	-1.45 ± 0.05
7	Non-Variable	-1.65	-1.54 ± 0.02	-1.39 ± 0.03
8	Variable	-1.71	-1.61 ± 0.03	-1.38 ± 0.04
9	Possible	-1.56	-1.44 ± 0.02	-1.44 ± 0.05
10	Non-Variable	-1.64	-1.56 ± 0.02	-1.42 ± 0.04
11	Non-Variable	-1.50	-1.40 ± 0.02	-1.42 ± 0.05
12	Non-Variable	-1.54	-1.43 ± 0.03	-1.43 ± 0.04
13	Non-Variable	-1.51	-1.45 ± 0.02	-1.45 ± 0.04
14	Non-Variable	-1.52	-1.50 ± 0.02	-1.45 ± 0.04
15	Non-Variable	-1.46	-1.44 ± 0.03	-1.44 ± 0.06
16	Possible	-1.59	-1.54 ± 0.02	-1.38 ± 0.04
17	Variable	-1.45	-1.31 ± 0.03	-1.29 ± 0.05

To further confirm our findings that stars that were possible variables and non-variables (except for Star N° 5) display iron abundances close to the mean, from Table 5.5 and from what was presented in Section 5.6.1, we calculated the mean abundance value for these stars:

- $\langle [\mathrm{Fe/H}] \rangle_{(\mathrm{Simmerer})} = -1.542 \pm 0.002$
- $\langle [\mathrm{Fe\ I/H}] \rangle_{(\mathrm{Mucciarelli})} = -1.477 \pm 0.007$
- $\langle [\mathrm{Fe\ II/H}] \rangle_{(\mathrm{Mucciarelli})} = -1.427 \pm 0.013$

The values shown from this calculation are close to the peak of the black-dashed histogram from Figure 5.9 and Figure 5.10, thus confirming our findings.

5.6.2. Discussion

From Figure 5.4 we can see that 3 variable stars (N° 4, 5 and 8) are AGB stars and the other 3 variables (N° 1, 2 and 17) are RGB stars. Furthermore, two out of the three AGB stars (Star N° 4 and Star N° 8) are the most metal-poor from the sample, which are the AGB stars discussed by A. Mucciarelli et al. (2015b) while the other AGB variable (Star N° 5) is the one that is neither extremely metal-poor nor metal-rich. We also note that all RGB variables are the most metal-rich stars. Furthermore, all possible variables are RGB stars, whereas the non-variables are either AGB or RGB, with the AGB stars (Star N° 7 and Star N° 10) being more metal-poor than the rest of the other non-variable, which is again consistent with what A. Mucciarelli et al. (2015b) found.

Moreover, from the results presented in Table 5.4, the amplitudes in V magnitude of each of the variable stars found could indicate that they are possibly SARVs or even ultra-small amplitude red variables (USARVs) due to the scale of our amplitues (for more information we invite to revise the comprehensive survey of GK giants from Henry et al. 2000), but due to the small timescale of our data and the periods obtained from our analysis we could not be certain to classify our variables as such. Same as with the case of the possible variable stars, longer and extensive photometric observations could help to improve our results by providing more complete light curves in order to be able to classify each of the variable stars found in this investigation and more importantly, to see if they present more than one period like typical PRGs.

5.6.3. Conclusion

From the results shown in Section 5.5 and Section 5.6.1 along with what was presented in Figures 5.9 and Figure 5.10, from the analysis of 34 light curves (17 in V and 17 in I filters) for 17 giant stars where 6 were classified as variable stars, 3 as possible variables and 8 as non-variable, the conclusion derived from this work is that there is a clear relation between the iron abundance and the variability of the giant stars, in the sense that variable stars display extreme values of [Fe I/H] (both metal-rich and metal-poor values). The metal-poor variables are AGB stars (as shown by A. Mucciarelli et al., 2015b) while the most metal-rich are RGB. This finding is consistent with the lone variable RGB star that was found in Muñoz et al. (2018). On the other hand stars that do not present variability display values of their iron abundance close to the mean metallicity of the total sample.

Chapter 6

Conclusions and Future Prospects

6.1. Summary and Conclusions

From the results provided in Llancaqueo Albornoz, et al. (submitted to MNRAS) with the study of 17 giant stars from the globular cluster NGC 3201 previously studied for their iron abundance, the conclusion from this work is that *a clear relation between the iron abundance and the variability of the giant stars* was found, where stars that are variable display extreme values of [Fe I/H], for both metal-rich and metal-poor values, compared to stars of the same cluster that are not variable which show abundances that are close to the mean metallicity of the total sample, which was proven by measuring the mean iron abundance of those specific stars. Moreover, from this work we discovered that stars that display more metal-poor are members of the asymptotic giant branch, while stars that display more metal-rich belong to the red giant branch. This conclusion opens a new approach on studying globular clusters, in the sense that we can combine spectroscopic observations to study chemical abundances and time series photometry on stars that belong to the giant branches.

6.2. Future works and prospects

Future prospects for this type of investigation would be to have more evidence for this results, in other words, check that NGC 3201 is not the only cluster that display the relationship that was found in this work. To acquire such evidence, more investigations of globular clusters that have detailed spectroscopic data of their giant stars, both RGB and AGB should be revised so that time series photometry should be done. Nowadays the VVV public survey is one of the best database for long-scale time series observations already available for globular clusters that are both in

the disk and bulge of the Galaxy. Some globular clusters candidates that should be investigated with this approach would be, for example, M22, M2, NGC 6528 and NGC 6440 which have already been analyzed spectroscopically by a number of authors. Also for the foreseeable future, the next step is to realize time series photometry and spectroscopic analysis on the variable giant stars to see if metallicity does change with the phase or not.

6.2.1. Latest works regarding [Fe/H] and variability

Investigations from Muñoz, et al. (2019, in preparation) shows chemical analysis of two bulge globular clusters, NGC 6569 and NGC 6553 where they found one star that presented variable behaviour in each cluster by analyzing time-series photometric data from the VVV survey using CASU aperture photometry.

Appendix A

Python code for the GLS and PDM analysis

Here the complete *Python* code that was employed for both the GLS and PDM analysis is presented using the packages from Sections 4.3.1 & 4.3.2, detailing each step in order to let the reader understand what the code does.

The first and most basic step when writing a *Python* code is to add the packages that will be used:

```
from __future__ import print_function, division
import numpy as np
import matplotlib.pylab as plt
from PyAstronomy.pyTiming import pyPeriod
from PyAstronomy.pyTiming import pyPDM
```

Next step is to load the data that will be analyzed. As in the case of this work the loaded data will be the light curves:

```
data= np.loadtxt('dat_wErrors-1581.510_0835.323V.txt')
#data= np.loadtxt('dat_wErrors-1591.517_0859.956I.txt')

time = data[:,0] #This variable corresponds to the column of the
    HJD
flux = data[:,1] #This variable corresponds to the column of the
    magnitudes
err = data[:,2] #This variable corresponds to the column of the
   magnitude errors
```

Note that there are two variables with the same name (data) but only one of these will be analyzed, to do this just type '#' on one of the variables to mark it as a 'comment' so that it will not be considered. After deciding which light curve will be analyzed first, we use the *PyAstronomy* module for the GLS analysis with the GLS class:

```
clp = pyPeriod.Gls((time, flux, err), norm="ZK", Pbeg=0.05, Pend
    =0.1)

```

```
clp.info() #This allows the code to print in the Terminal the
    statistical results

#Define FAP levels of 10%, 5%, 1% and 0.1%
fapLevels = np.array([0.1, 0.05, 0.01, 0.001])
plevels = clp.powerLevel(fapLevels)
```

From this part of the code, the parameter *norm="ZK"* is to compute the GLS periodogram using the Zechmeister-Kuerster normalization. The last lines that were shown are used to add the False Alarm Probability levels (see Section 4.1.1), which are used to check which periods are spurious and which are significant. To compute the FAP, the user has to create an array with all the FAP levels desired to be considered in decimal values (e.g. 0.1 being 10%, 0.01 being 1%, etc.). The value of "Prob$(P > P_n)$" depends on the normalization used (*norm*) and the value of M is computed internally in the program.

```
#Get index associated with highest power
ifmax = np.argmax(clp.power)

pmax = clp.power[ifmax]
fmax = clp.freq[ifmax]

hpp = 1./fmax
print("Highest-power period: ", hpp) #Define a variable equal to
    the highest-power period and print it

freqstep=clp.fstep #Define a variable equal to the frequency
    step
periodos= (1./clp.freq) #Define a variable equal to the periods
    that will be evaluated
```

The statistic results that the code presents are shown in Figure A.1[1].

After finishing the GLS analysis the code begins using the *PyAstronomy* module for the PDM analysis:

```
S = pyPDM.Scanner(minVal=(1./clp.Pend), maxVal=(1./clp.Pbeg),
    dVal=freqstep, mode="frequency")

P = pyPDM.PyPDM(time, flux) #This line allows the code to
    perform the PDM method

f1, t1 = P.pdmEquiBinCover(10, 3, S) #Define the frequencies and
    the theta values that will
                                    #be evaluated in the PDM
    method

```

[1]The amplitude (which we refer as A_{GLS}) that the program calculates correspond to half of the sinusoidal fit amplitude, in this work the presented amplitudes in the results (Section 5.5) are the full sinusoidal fit amplitude, or $A = 2A_{GLS}$

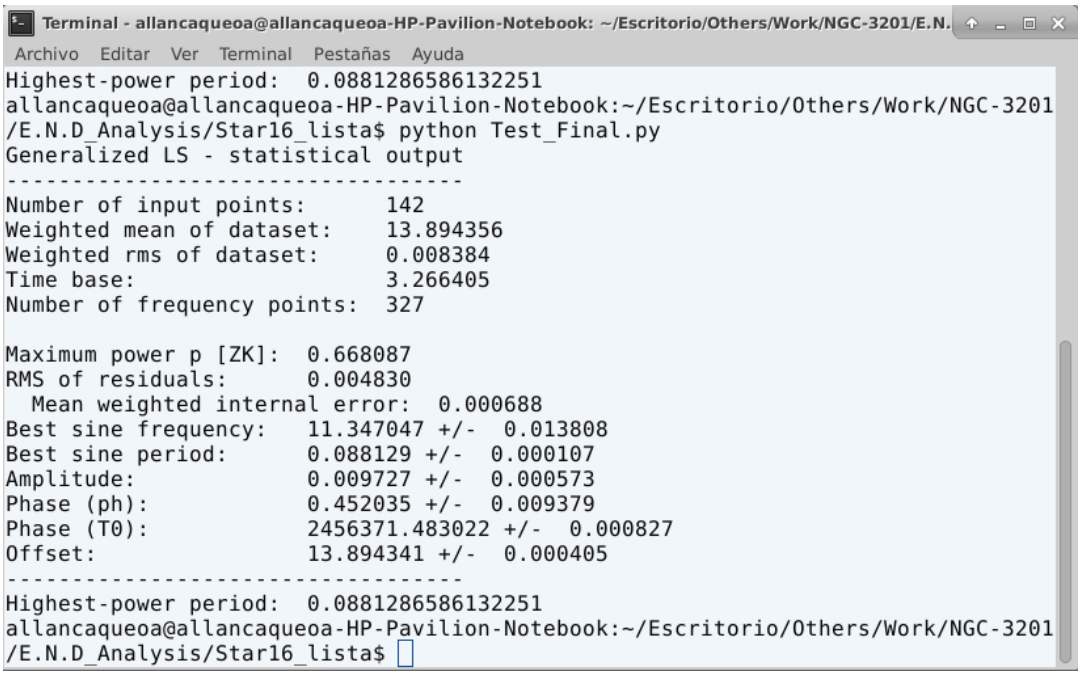

FIGURE A.1: Printed statistical results with the highest-power period obtained from the GLS periodogram analysis in the Terminal. In this case, the analyzed light curve for Star N° 8 in the *V* filter.

```
#Finding the minimum value of Theta
thetmin1=np.min(t1)

equis= np.linspace(0, 10.0, 2)
lequis=np.array([thetmin1 for i in range(len(equis))])

periodo1 = (1/f1) #Define the periods as 1/frequencies

np.savetxt('periodos.txt', zip(periodo1), fmt='%.18f') #We save
    all the periods in a .txt file
```

Finally, the results for both analysis are plotted in one image consisting of one column and two rows (2,1) with the top plot being the result from the GLS analysis and the bottom plot the result from the PDM analysis:

```
#Plot for the results of the GLS periodogram
plt.subplot(2,1,1)
plt.plot((1./clp.freq), clp.power, 'b.-')
for i in range(len(fapLevels)):
    plt.plot([min(1./clp.freq), max(1./clp.freq)], [plevels[i]]*
    2, '--',
    label="FAP = %4.1f%%" % (fapLevels[i]*100))
plt.xlabel("Period")
plt.ylabel("Power")
plt.xlim(clp.Pbeg,clp.Pend)
plt.grid()

#Plot for the results of the PDM method
```

```
plt.subplot(2,1,2)
plt.plot(periodo1, t1, 'kp-')
plt.plot(equis, lequis, color='black', linestyle='--')
plt.grid()
plt.xlabel("Period")
plt.ylabel("$\Theta$")
plt.xlim(clp.Pbeg,clp.Pend)
plt.show()
```

After performing the analysis of the light curve for one filter, the # that was written on one of the variables 'data' is deleted and then typed on the other 'data'. The resulting plots from the code are shown in Figure. A.2 with the top panels being the results from the GLS analysis and the bottom panels being the results from the PDM analysis. In the top panels there are four colored dashed lines, which are the different FAP levels, with blue being 10%, orange 5%, green 1% and red 0.1% significance. For the bottom panels, the dashed line is to display the position of the minimum value of Θ, in case that there are multiple peaks with similar values.

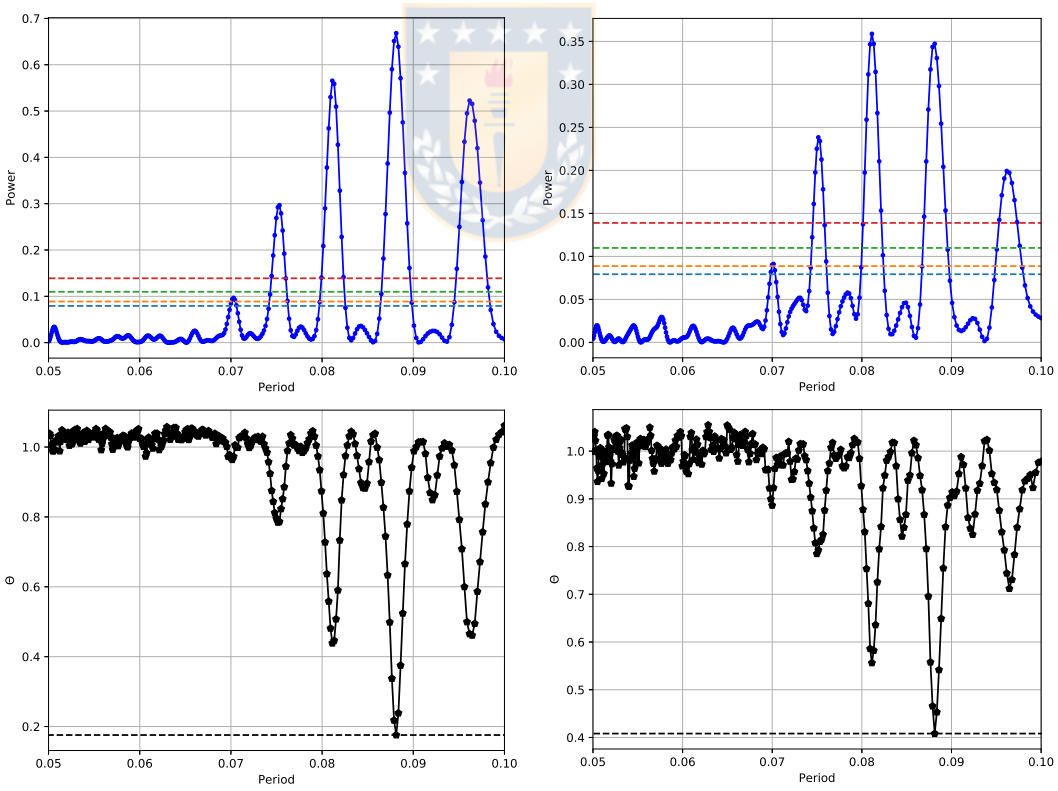

(A) Plots from the GLS and PDM analysis for *V* filter

(B) Plots from the GLS and PDM analysis for *I* filter

FIGURE A.2: Resulting plots from the GLS and PDM analysis performed with the *Python* code previously detailed. Both results are from the analysis of Star N°8.

Appendix B

Python code for the Phase Curves

Similar to the code from Appendix A, the first step is to load the packages and libraries that are going to be used, along with the archives that will be necessary to create the plots, for the example code that will be displayed the data will be from the same star as in the previous sample of the code from the GLS and PDM analysis, being Star N° 8. A difference with the previous code is that, instead of loading the complete light curve data in one single archive, the data corresponding to each night of observation was separated in order to plot the data of each night with a different color:

```
import numpy as np
import matplotlib.pylab as plt

#Load the data corresponding to the V filter for each separate
    night
dataV1= np.loadtxt('data_star8V_noche1.txt')
dataV2= np.loadtxt('data_star8V_noche2.txt')
dataV3= np.loadtxt('data_star8V_noche3.txt')
dataV4= np.loadtxt('data_star8V_noche4.txt')

timeV1 = dataV1[:,0]  #Assigning a variable for the HJD and
    Magnitude for each individual night
fluxV1 = dataV1[:,1]

timeV2 = dataV2[:,0]
fluxV2 = dataV2[:,1]

timeV3 = dataV3[:,0]
fluxV3 = dataV3[:,1]

timeV4 = dataV4[:,0]
fluxV4 = dataV4[:,1]

#And for the I filter
dataI1= np.loadtxt('data_star8I_noche1.txt')
```

```
dataI2= np.loadtxt('data_star8I_noche2.txt')
dataI3= np.loadtxt('data_star8I_noche3.txt')
dataI4= np.loadtxt('data_star8I_noche4.txt')

timeI1 = dataI1[:,0]
fluxI1 = dataI1[:,1]

timeI2 = dataI2[:,0]
fluxI2 = dataI2[:,1]

timeI3 = dataI3[:,0]
fluxI3 = dataI3[:,1]

timeI4 = dataI4[:,0]
fluxI4 = dataI4[:,1]


per1= 0.0881286586132251     #Create a variable equal to the
    period found by the GLS and PDM analysis
```

Finally, 2 row-1 column multiplot is made with the top panel being the phased light curve for *V* filter and the bottom panel the phased light curve for *I* filter, each plot going from -0.6 to 2.06 in the x-axis to have a clear view of the form of the phase curve::

```
plt.subplot(2,1,1) #Plot corresponding to the phased light curve
    for V filter

plt.plot(((timeV1/per1)-000.0-np.floor((timeV1/per1)-000.0)),
    fluxV1, 'g.', label='Night 1')
plt.plot(((timeV2/per1)-000.0-np.floor((timeV2/per1)-000.0)),
    fluxV2, 'c.', label='Night 2')
plt.plot(((timeV3/per1)-000.0-np.floor((timeV3/per1)-000.0)),
    fluxV3, 'y.', label='Night 3')
plt.plot(((timeV4/per1)-000.0-np.floor((timeV4/per1)-000.0)),
    fluxV4, 'b.', label='Night 4')
plt.plot(((timeV1/per1)-000.0-np.floor((timeV1/per1)-000.0))
    +1.0, fluxV1, 'g.')
plt.plot(((timeV2/per1)-000.0-np.floor((timeV2/per1)-000.0))
    +1.0, fluxV2, 'c.')
plt.plot(((timeV3/per1)-000.0-np.floor((timeV3/per1)-000.0))
    +1.0, fluxV3, 'y.')
plt.plot(((timeV4/per1)-000.0-np.floor((timeV4/per1)-000.0))
    +1.0, fluxV4, 'b.')
plt.xlim(-0.06,2.06)
plt.grid()
plt.ylim(plt.ylim()[::-1])
plt.ylabel('$V$')

#-------------------------------
plt.subplot(2,1,2) #Plot corresponding to the phased light curve
    for I filter
```

```
18
19 plt.plot(((timeI1/per1)-000.0-np.floor((timeI1/per1)-000.0)),
       fluxI1, 'r.', label='Night 1')
20 plt.plot(((timeI2/per1)-000.0-np.floor((timeI2/per1)-000.0)),
       fluxI2, 'm.', label='Night 2')
21 plt.plot(((timeI3/per1)-000.0-np.floor((timeI3/per1)-000.0)),
       fluxI3, color='orangered', marker='.', label='Night 3',
       linewidth=0)
22 plt.plot(((timeI4/per1)-000.0-np.floor((timeI4/per1)-000.0)),
       fluxI4, color='purple',marker='.', label='Night 4',linewidth
       =0)
23 plt.plot((((timeI1/per1)-000.0-np.floor((timeI1/per1)-000.0)))
       +1.0, fluxI1, 'r.')
24 plt.plot((((timeI2/per1)-000.0-np.floor((timeI2/per1)-000.0)))
       +1.0, fluxI2, 'm.')
25 plt.plot((((timeI3/per1)-000.0-np.floor((timeI3/per1)-000.0)))
       +1.0, fluxI3, color='orangered',marker='.',linewidth=0)
26 plt.plot((((timeI4/per1)-000.0-np.floor((timeI4/per1)-000.0)))
       +1.0, fluxI4, color='purple',marker='.',linewidth=0)
27 plt.xlim(-0.06,2.06)
28 plt.grid()
29 plt.ylim(plt.ylim()[::-1])
30 plt.ylabel('$I$')
31 plt.xlabel('$\phi$')
32
33 plt.show()
```

Depending on the star, the phase would be shifted differently by modifying the decimal part of the number 000.0 in each corresponding line, so that the resulting phased light curve can be appreciated in a better way. The resulting plots are the ones seen in Figure 5.5, Figure 5.6, Figure 5.7 and Figure 5.8

Bibliography

Arellano Ferro, A. et al. (2014). "Fourier Decomposition of RR Lyrae light curves and the SX Phe population in the central region of NGC 3201". In: *RMxAA* 50, pp. 307–322. arXiv: 1406.2635 [astro-ph.SR].

Asplund, Martin et al. (2009). "The Chemical Composition of the Sun". In: *ARA&A* 47.1, pp. 481–522. DOI: 10.1146/annurev.astro.46.060407.145222. arXiv: 0909.0948 [astro-ph.SR].

Bekki, K. and K. C. Freeman (2003). "Formation of ω Centauri from an ancient nucleated dwarf galaxy in the young Galactic disc". In: *MNRAS* 346.2, pp. L11–L15. DOI: 10.1046/j.1365-2966.2003.07275.x. arXiv: astro-ph/0310348 [astro-ph].

Bellazzini, M. et al. (2008). "The Nucleus of the Sagittarius Dsph Galaxy and M54: a Window on the Process of Galaxy Nucleation". In: *AJ* 136.3, pp. 1147–1170. DOI: 10.1088/0004-6256/136/3/1147. arXiv: 0807.0105 [astro-ph].

Bergemann, Maria et al. (2012). "Non-LTE line formation of Fe in late-type stars - I. Standard stars with 1D and <3D> model atmospheres". In: *MNRAS* 427.1, pp. 27–49. DOI: 10.1111/j.1365-2966.2012.21687.x. arXiv: 1207.2455 [astro-ph.SR].

Bertulani, Carlos A (2013). *Nuclei in the Cosmos*. WORLD SCIENTIFIC. DOI: 10.1142/8573. eprint: https://www.worldscientific.com/doi/pdf/10.1142/8573. URL: https://www.worldscientific.com/doi/abs/10.1142/8573.

Bramich, D. M. (2008). "A new algorithm for difference image analysis". In: *MNRAS* 386.1, pp. L77–L81. DOI: 10.1111/j.1745-3933.2008.00464.x. arXiv: 0802.1273 [astro-ph].

Bramich, D. M. and W. Freudling (2012). "Systematic trends in Sloan Digital Sky Survey photometric data". In: *MNRAS* 424.2, pp. 1584–1599. DOI: 10.1111/j.1365-2966.2012.21385.x. arXiv: 1205.5409 [astro-ph.IM].

Bramich, D. M. et al. (2013). "Difference image analysis: extension to a spatially varying photometric scale factor and other considerations". In: *MNRAS* 428.3, pp. 2275–2289. DOI: 10.1093/mnras/sts184. arXiv: 1210.2926 [astro-ph.IM].

Cannon, R. D. and R. S. Stobie (1973). "Photometry of Southern globular clusters. I. Bright stars in OME Cen." In: *MNRAS* 162, p. 207. DOI: 10.1093/mnras/162.3.207.

Carretta, E. et al. (2009a). "Intrinsic iron spread and a new metallicity scale for globular clusters". In: *A&A* 508.2, pp. 695–706. DOI: 10.1051/0004-6361/200913003. arXiv: 0910.0675 [astro-ph.GA].

Carretta, E. et al. (2009b). "Na-O anticorrelation and HB. VII. The chemical composition of first and second-generation stars in 15 globular clusters from GIRAFFE spectra". In: *A&A* 505.1, pp. 117–138. DOI: 10.1051/0004-6361/200912096. arXiv: 0909.2938 [astro-ph.GA].

Carretta, E. et al. (2009c). "Na-O anticorrelation and HB. VIII. Proton-capture elements and metallicities in 17 globular clusters from UVES spectra". In: *A&A* 505.1, pp. 139–155. DOI: 10.1051/0004-6361/200912097. arXiv: 0909.2941 [astro-ph.GA].

Catelan, M. and H. A. Smith (2015). *Pulsating Stars*.

Da Costa, G. S., E. V. Held, and I. Saviane (2014). "NGC 5824: a luminous outer halo globular cluster with an intrinsic abundance spread". In: *MNRAS* 438.4, pp. 3507–3520. DOI: 10.1093/mnras/stt2467. arXiv: 1312.5796 [astro-ph.SR].

D'Antona, F. et al. (2002). "Helium variation due to self-pollution among Globular Cluster stars. Consequences on the horizontal branch morphology". In: *A&A* 395, pp. 69–75. DOI: 10.1051/0004-6361:20021220. arXiv: astro-ph/0209331 [astro-ph].

D'Antona, F. et al. (2016). "A single model for the variety of multiple-population formation(s) in globular clusters: a temporal sequence". In: *MNRAS* 458.2, pp. 2122–2139. DOI: 10.1093/mnras/stw387. arXiv: 1602.05412 [astro-ph.GA].

de Mink, S. E. et al. (2010). "Massive binaries and the enrichment of the interstellar medium in globular clusters". In: *Star Clusters: Basic Galactic Building Blocks Throughout Time and Space*. Ed. by Richard de Grijs and Jacques R. D. Lépine. Vol. 266. IAU Symposium, pp. 169–174. DOI: 10.1017/S1743921309991025. arXiv: 0910.3767 [astro-ph.SR].

Decressin, T., C. Charbonnel, and G. Meynet (2007). "Origin of the abundance patterns in Galactic globular clusters: constraints on dynamical and chemical properties of globular clusters". In: *A&A* 475.3, pp. 859–873. DOI: 10.1051/0004-6361:20078425. arXiv: 0709.4160 [astro-ph].

Eggen, O. J. (1972). "The classification of intrinsic variable star. II. The red variables of S and related types." In: *ApJ* 177, p. 489. DOI: 10.1086/151725.

— (1973a). "The classification of intrinsic variables. Calibration of luminosities of small amplitude red variables in the old disk population." In: *ApJ* 180, p. 857. DOI: 10.1086/152012.

— (1973b). "The classification of intrinsic variables.4 Very-small-amplitude, very-short-period red variables." In: *ApJ* 184, p. 793. DOI: 10.1086/152371.

— (1975a). "Classification of intrinsic variables. VI. Ultrashort period, very small amplitude B-type variables." In: *ApJ* 198, pp. 131–138. DOI: 10.1086/153584.

— (1975b). "The classification of intrinsic variables. V. The large-amplitude variables." In: *ApJ* 195, pp. 661–678. DOI: 10.1086/153367.

— (1977). "The classification of intrinsic variables. VII. The medium-amplitude red variables." In: *ApJ* 213, pp. 767–786. DOI: 10.1086/155206.

Ferraro, F. R. et al. (2016). "The Age of the Young Bulge-like Population in the Stellar System Terzan 5: Linking the Galactic Bulge to the High-z Universe". In: *ApJ* 828.2, 75, p. 75. DOI: 10.3847/0004-637X/828/2/75. arXiv: 1609.01515 [astro-ph.GA].

Freeman, K. C. and A. W. Rodgers (1975). "The Chemical Inhomogeneity of Omega Centauri". In: *ApJL* 201, p. L71. DOI: 10.1086/181945.

Geyer, E. H. (1967). "Eine Dreifarbenphotometrie von Omega Centauri (NGC 5139)". In: *Z. Astrophys* 66, p. 16.

Gonzalez, Guillermo and George Wallerstein (1998). "Elemental Abundances in Giants in NGC 3201, a Globular Cluster with a Retrograde Orbit". In: *AJ* 116.2, pp. 765–781. DOI: 10.1086/300476.

Gratton, Raffaele, Christopher Sneden, and Eugenio Carretta (2004). "Abundance Variations Within Globular Clusters". In: *ARA&A* 42.1, pp. 385–440. DOI: 10.1146/annurev.astro.42.053102.133945.

Harris, W. E. (1996). "A Catalog of Parameters for Globular Clusters in the Milky Way". In: *AJ* 112, p. 1487. DOI: 10.1086/118116.

Henry, Gregory W. et al. (2000). "Photometric Variability in a Sample of 187 G and K Giants". In: *ApJS* 130.1, pp. 201–225. DOI: 10.1086/317346.

Johnson, Christian I. et al. (2016). "The Chemical Composition of Red Giant Branch Stars in the Galactic Globular Clusters NGC 6342 and NGC 6366". In: *AJ* 152.1, 21, p. 21. DOI: 10.3847/0004-6256/152/1/21. arXiv: 1606.08491 [astro-ph.SR].

Kippenhahn, R. (1965). "A Hydrogen Exhaustion, Helium Burning Carbon flash and Mass Loss". In: *Mitteilungen der Astronomischen Gesellschaft Hamburg* 19, p. 53.

Lafler, J. and T. D. Kinman (1965). "An RR Lyrae Star Survey with Ihe Lick 20-INCH Astrograph II. The Calculation of RR Lyrae Periods by Electronic Computer." In: *ApJS* 11, p. 216. DOI: 10.1086/190116.

Lamers, Henny J. G. L. M. and Emily M. Levesque (2017). *Understanding Stellar Evolution*. DOI: 10.1088/978-0-7503-1278-3.

Landolt, A. U. (1973). "UBV photoelectric sequences in the celestial equatorial Selected Areas 92-115." In: *AJ* 78, pp. 959–981. DOI: 10.1086/111503.

Lapenna, E. et al. (2014). "Non-local Thermodynamical Equilibrium Effects on the Iron Abundance of Asymptotic Giant Branch Stars in 47 Tucanae". In: *ApJ* 797.2, 124, p. 124. DOI: 10.1088/0004-637X/797/2/124.

Lardo, C., A. Mucciarelli, and N. Bastian (2016). "The iron dispersion of the globular cluster M2, revised". In: *MNRAS* 457.1, pp. 51–63. DOI: 10.1093/mnras/stv2802. arXiv: 1512.00691 [astro-ph.SR].

Layden, Andrew C. and Ata Sarajedini (2003). "Photometry of the Globular Cluster NGC 3201 and Its Variable Stars". In: *AJ* 125.1, pp. 208–223. DOI: 10.1086/344948.

Lind, K., M. Bergemann, and M. Asplund (2012). "Non-LTE line formation of Fe in late-type stars - II. 1D spectroscopic stellar parameters". In: *MNRAS* 427.1, pp. 50–60. DOI: 10.1111/j.1365-2966.2012.21686.x. arXiv: 1207.2454 [astro-ph.SR].

Lomb, N. R. (1976). "Least-Squares Frequency Analysis of Unequally Spaced Data". In: *Astrophysics and Space Science* 39.2, pp. 447–462. DOI: 10.1007/BF00648343.

Marino, A. F. et al. (2009). "A double stellar generation in the globular cluster NGC 6656 (M 22). Two stellar groups with different iron and s-process element abundances". In: *A&A* 505.3, pp. 1099–1113. DOI: 10.1051/0004-6361/200911827. arXiv: 0905.4058 [astro-ph.SR].

Marino, A. F. et al. (2011a). "Sodium-Oxygen Anticorrelation and Neutron-capture Elements in Omega Centauri Stellar Populations". In: *ApJ* 731.1, 64, p. 64. DOI: 10.1088/0004-637X/731/1/64. arXiv: 1102.1653 [astro-ph.SR].

Marino, A. F. et al. (2011b). "The two metallicity groups of the globular cluster M 22: a chemical perspective". In: *A&A* 532, A8, A8. DOI: 10.1051/0004-6361/201116546. arXiv: 1105.1523 [astro-ph.SR].

Marino, A. F. et al. (2015). "Iron and s-elements abundance variations in NGC 5286: comparison with 'anomalous' globular clusters and Milky Way satellites". In: *MNRAS* 450.1, pp. 815–845. DOI: 10.1093/mnras/stv420. arXiv: 1502.07438 [astro-ph.SR].

Minniti, D. et al. (2010). "VISTA Variables in the Via Lactea (VVV): The public ESO near-IR variability survey of the Milky Way". In: *New Astronomy* 15.5, pp. 433–443. DOI: 10.1016/j.newast.2009.12.002. arXiv: 0912.1056 [astro-ph.GA].

Muñoz, C., D. Geisler, and S. Villanova (2013). "The origin and chemical evolution of the exotic globular cluster NGC 3201". In: *MNRAS*

433.3, pp. 2006–2017. DOI: 10.1093/mnras/stt868. arXiv: 1305.3645 [astro-ph.GA].

Muñoz, C. et al. (2018). "Chemical analysis of NGC 6528: one of the most metal-rich bulge globular clusters". In: *A&A* 620, A96, A96. DOI: 10.1051/0004-6361/201833373. arXiv: 1809.04164 [astro-ph.SR].

Mucciarelli, Alessio et al. (2018). "The Chemical Composition of NGC 5824, a Globular Cluster without Iron Spread but with an Extreme Mg-Al Anticorrelation". In: *ApJ* 859.1, 75, p. 75. DOI: 10.3847/1538-4357/aaba80. arXiv: 1803.09759 [astro-ph.SR].

Mucciarelli, A. et al. (2015a). "A Chemical Trompe-L'oeil: No Iron Spread in the Globular Cluster M22". In: *ApJ* 809.2, 128, p. 128. DOI: 10.1088/0004-637X/809/2/128. arXiv: 1507.01596 [astro-ph.SR].

Mucciarelli, A. et al. (2015b). "The Origin of the Spurious Iron Spread in the Globular Cluster NGC 3201". In: *ApJ* 801.1, 69, p. 69. DOI: 10.1088/0004-637X/801/1/69. arXiv: 1501.01968 [astro-ph.SR].

Mucciarelli, A. et al. (2017). "Chemical abundances in the nucleus of the Sagittarius dwarf spheroidal galaxy". In: *A&A* 605, A46, A46. DOI: 10.1051/0004-6361/201730707. arXiv: 1705.03251 [astro-ph.GA].

Origlia, Livia et al. (2003). "A Near-Infrared Spectroscopic Screening of the Red Giant Populations in ω Centauri". In: *ApJ* 591.2, pp. 916–924. DOI: 10.1086/375363. arXiv: astro-ph/0303601 [astro-ph].

Origlia, L. et al. (2011). "Spectroscopy Unveils the Complex Nature of Terzan 5". In: *ApJL* 726.2, L20, p. L20. DOI: 10.1088/2041-8205/726/2/L20. arXiv: 1012.2047 [astro-ph.GA].

Origlia, L. et al. (2013). "The Terzan 5 Puzzle: Discovery of a Third, Metal-poor Component". In: *ApJL* 779.1, L5, p. L5. DOI: 10.1088/2041-8205/779/1/L5. arXiv: 1311.1706 [astro-ph.GA].

Pancino, E. et al. (2011). "The subgiant branch of ω Centauri seen through high-resolution spectroscopy. I. The first stellar generation in ω Cen?" In: *A&A* 527, A18, A18. DOI: 10.1051/0004-6361/201016024. arXiv: 1012.4756 [astro-ph.SR].

Renzini, Alvio and Flavio Fusi Pecci (1988). "Tests of evolutionary sequences using color-magnitude diagrams of globular clusters." In: *ARA&A* 26, pp. 199–244. DOI: 10.1146/annurev.aa.26.090188.001215.

Saito, R. K. et al. (2012). "VVV DR1: The first data release of the Milky Way bulge and southern plane from the near-infrared ESO public survey VISTA variables in the Vıa Láctea". In: *A&A* 537, A107, A107. DOI: 10.1051/0004-6361/201118407. arXiv: 1111.5511 [astro-ph.GA].

Salaris, M. and S. Cassisi (2005). *Evolution of Stars and Stellar Populations*, p. 400.

Samus', N. N. et al. (2017). "General catalogue of variable stars: Version GCVS 5.1". In: *Astronomy Reports* 61, pp. 80–88. DOI: 10.1134/S1063772917010085.

Scargle, J. D. (1982). "Studies in astronomical time series analysis. II. Statistical aspects of spectral analysis of unevenly spaced data." In: *ApJ* 263, pp. 835–853. DOI: 10.1086/160554.

Simmerer, Jennifer et al. (2013). "Star-to-star Iron Abundance Variations in Red Giant Branch Stars in the Galactic Globular Cluster NGC 3201". In: *ApJL* 764.1, L7, p. L7. DOI: 10.1088/2041-8205/764/1/L7.

Stellingwerf, R. F. (1978). "Period determination using phase dispersion minimization." In: *ApJ* 224, pp. 953–960. DOI: 10.1086/156444.

Stetson, Peter B. (2000). "Homogeneous Photometry for Star Clusters and Resolved Galaxies. II. Photometric Standard Stars". In: *PASP* 112.773, pp. 925–931. DOI: 10.1086/316595. arXiv: astro-ph/0004144 [astro-ph].

Villanova, S. et al. (2013). "Ruprecht 106: The First Single Population Globular Cluster?" In: *ApJ* 778.2, 186, p. 186. DOI: 10.1088/0004-637X/778/2/186. arXiv: 1310.5900 [astro-ph.GA].

von Braun, Kaspar and Mario Mateo (2001). "An Extinction Map and Color-Magnitude Diagram for the Globular Cluster NGC 3201". In: *AJ* 121.3, pp. 1522–1532. DOI: 10.1086/319406. arXiv: astro-ph/0011560 [astro-ph].

Wood, P. R., E. A. Olivier, and S. D. Kawaler (2004). "Long Secondary Periods in Pulsating Asymptotic Giant Branch Stars: An Investigation of their Origin". In: *ApJ* 604.2, pp. 800–816. DOI: 10.1086/382123.

Yong, David et al. (2014). "Iron and neutron-capture element abundance variations in the globular cluster M2 (NGC 7089)". In: *MNRAS* 441.4, pp. 3396–3416. DOI: 10.1093/mnras/stu806. arXiv: 1404.6873 [astro-ph.SR].

Zechmeister, M. and M. Kürster (2009). "The generalised Lomb-Scargle periodogram. A new formalism for the floating-mean and Keplerian periodograms". In: *A&A* 496.2, pp. 577–584. DOI: 10.1051/0004-6361:200811296. arXiv: 0901.2573 [astro-ph.IM].